Nonlinear numerical simulation of the soil seismic response to the 2012 Mw 5.9 Emilia earthquake considering the variability of the water table position

Maria Paola Santisi d'Avila, Luca Lenti, Salvatore Martino

HAL Id: hal-02613232
https://hal.science/hal-02613232

Submitted on 19 May 2020

1 **Nonlinear numerical simulation of the soil seismic response to the 2012 Mw 5.9 Emilia**

2 **earthquake considering the variability of the water table position**

3

4 Maria Paola Santisi d'Avila[1], Luca Lenti[2], Salvatore Martino[3] and Roberto Walter Romeo[4+]

5

6 [1] Université Côte d'Azur, LJAD, Nice, France

7 [2] Université Paris Est, IFSTTAR, Paris, France

8 [3] Università Roma La Sapienza, CERI, Roma, Italy

9 [4] Libera Università di Urbino Carlo Bo, Urbino, Italy

10 [+] deceased

11

12

13 Corresponding author:

14 Maria Paola Santisi d'Avila

15 Université Côte d'Azur - LJAD

16 28, Avenue Valrose - 06108 Nice - France

17 Email: msantisi@unice.fr

18

ABSTRACT

This research is focused on the case study of San Carlo village (Emilia Romagna, Italy), struck by the 20 May 2012 Mw 5.9 Emilia earthquake that caused severe damage due to widely observed soil liquefaction. More in particular, it is investigated the influence on nonlinearity effects of the variability of the water table depth, due to seasonal fluctuation.

The one-directional propagation of a three-component seismic wave (1D-3C approach), in a multilayered soil profile, is simulated using a finite element model and an elasto-plastic constitutive behavior with hardening for the soil (Iwan's model). The nonlinearity is described by the normalized shear modulus decay curve obtained by resonant column tests. The shear modulus is corrected during the process (Iai's model) to consider the cyclic mobility and dilatancy of sands, depending on the actual average effective stress and the friction and dilatancy angles obtained from cyclic consolidated undrained triaxial tests.

Profiles with depth of maximum excess pore water pressure, horizontal motion and shear strain and stress are obtained in the case of effective stress analysis, for an average position of the water table depth and for a variation of ± 1 m, and then compared with a total stress analysis. The variability with the water table depth of soil profile response to seismic loading is observed also in terms of hysteresis loops, time histories of the ground motion and excess pore water pressure in the liquefiable soil layers prone to cyclic mobility process.

Keywords: saturated soil, liquefaction front, wave propagation, Finite Element Method, Emilia earthquake.

INTRODUCTION

During the 20 May 2012 Mw 5.9 Emilia earthquake (Italy), liquefaction phenomena have been observed (Chini et al., 2015; Emergeo Working Group, 2013). Several studies (Facciorusso et al. 2014, 2015; Vannucchi et al., 2012; Papathanassiou et al., 2015) demonstrate that predisposing conditions to soil liquefaction could be recognized in several sites (including the villages of San Carlo, Mirabello and Sant'Agostino) where such an effect was induced by the 2012 Emilia earthquake. Focusing on this case study, the impact of water table depth on the earthquake-induced effects in soil columns is here analyzed.

Effects due to co-seismic water level changes, inducing soil liquefaction, are observed and discussed by Wang et al. (2003) while Wayne and Dohering (2006) observe liquefaction induced by measured water level changes after detonation in underground of chemical and nuclear explosives. Some authors (Nishikawi et al., 2009; Yasuda and Ishikawa, 2015) discuss the possible role of water table lowering for the soil improvement against co-seismic liquefaction occurrence and building damage. Moreover, a co-relation of shallow groundwater levels with the liquefaction occurrence is proposed by Hartantyo et al., 2014 for the May 2006 Earthquake at Yogyakarta (Indonesia). Some analytical evaluations are performed to consider the effect of water level on analytical indexes for liquefaction susceptibly as well as on induced post-seismic settlements (Chung and Rogers, 2013).

In this research, a numerical modeling is developed to simulate the seismic response of the soil columns through effective stress analysis (ESA). A vertical wave propagation model is adopted under the assumption of horizontally extended soil. The one-directional (1D) wave propagation modeling, compared with a three-dimensional (3D) one, reduces modeling difficulties and computation time, and guarantees a reliable geotechnical model, easy to characterize with

65   limited geotechnical investigations. The finite element model adopted to simulate the

66   propagation of three-component (3C) seismic waves, in a multilayered subsoil, is implemented

67   in SWAP_3C code (Santisi et al., 2012) that has been verified and validated during the

68   PRENOLIN benchmark (Regnier et al., 2018) in the case of total stress analysis (TSA) and

69   nonlinear soil behavior.

70   The Iwan's elasto-plastic model (Iwan, 1967; Joyner, 1975; Joyner and Chen, 1975) is adopted

71   to represent the 3D nonlinear behavior of soil. Its main feature is the faithful reproduction of

72   nonlinear and hysteretic behavior of soils under cyclic loadings, with a reduced number of

73   parameters characterizing the soil properties. The model is calibrated using the elastic moduli in

74   shear and compression and the shear modulus decay curve is employed to deduce the size of the

75   yield surface.

76   The correction of the shear modulus proposed by Iai et al. (1990a,b) is employed for saturated

77   cohesionless soil layers to consider the cyclic mobility and dilatancy of sands. Liquefaction front

78   parameters are calibrated by a trial-and-error procedure to best reproduce the curves obtained by

79   cyclic consolidated undrained triaxial (CTX) tests, that represent the deviatoric strain amplitude

80   and normalized excess pore water pressure with respect to the number of cyclic loading. Bonilla

81   *et al.* (2005) propose the Iwan's hysteretic model combined with the Iai's liquefaction front

82   model. The model is applied to a one-directional one-component seismic wave propagation, in a

83   finite difference formulation. Oral *et al.* (2017) use the extension of Iai's shear modulus

84   correction to a multiaxial stress state, induced by a 3C excitation. The model is adopted in a

85   spectral element formulation, for a three-component seismic loading propagating in a 1D soil

86   profile. Santisi d'Avila et al. (2018) discuss the 3D Iwan-Iai model and compare the behavior of

87   dense and loose sands under one- and three-component loading. They also validate the one-

88   directional three-component (1D-3C) wave propagation model in liquefiable soils, for the case

89   of KSRH10 Japanese soil profile, whose geotechnical data are provided by the reports of

90   PRENOLIN benchmark.

91   Stratigraphy and geotechnical parameters of three soil profiles in San Carlo village (Emilia

92   Romagna, Italy) are accurately identified based on available data and specifically performed

93   borehole investigations. The simulation of their response to the 20 May 2012 Mw 5.9 Emilia

94   earthquake is initially performed by considering an average depth of the water table. In the

95   following, the influence of the water table depth variability on the seismic response of the

96   investigated soil profiles is accounted for and the obtained results are discussed, in terms of

97   ground motion at the surface and profiles with depth of maximum stress, strain and soil motion.

98   The case study is of particular interest for the Italian National Civil Protection since it pointed

99   out emergency conditions induced by liquefaction effects. Moreover, due to the similarity of

100   geological setting of the area felt by the 2012 Emilia earthquake with large zones of the Pianura

101   Padana plain (northern Italy) this case study exemplifies conditions that could be somewhere

102   else expected.

103   Due to the co-seismic nature of the nonlinear effects related to soil liquefaction, this study

104   contributes to depict quantitative provisional scenarios for risk mitigation by identifying

105   geological setting prone to liquefaction and supporting the outline of unstable zones in the

106   framework of Seismic Microzonation studies (DPC-CRP, 2008).

107

108   **CASE STUDY**

109   On May 2012 a seismic sequence hit the river Po valley plain in Northern Italy, with two

110   mainshocks of magnitude close to 6 (Scognamiglio et al., 2012) which triggered several ground

111 effects mainly represented by liquefaction (Fig. 1a,b) in all its variegated phenomena (i.e. sand

112 boils crack fissures, lateral spreading, settlements). Such effects significantly contributed to

113 increase the structural damages due to the seismic shaking (Fig. 1c,d).

114 The investigated site was shaken by earthquakes of similar magnitude which produced similar

115 ground effects in the past (Martino et al., 2014), as reported in the Italian catalogue of

116 earthquake-induced ground effects (CEDIT, see Data and Resources). The seismic sequence,

117 well described in Scognamiglio et al. (2012), consisted of two mainshocks, the first of which

118 (M_w 5.9 on May 20th, 2012) was responsible for the liquefaction effects at the investigated site

119 (16 km far from the epicentre). The inferred peak ground acceleration according to the

120 automated shakemaps (INGV, see Data and Resources) is about $0.32\,g$.

121 After the seismic sequence, many investigations are carried out, both on site and in laboratory,

122 in order to explore the soil susceptibility to undergo failure. Some studies are already published

123 attempting to explain the triggering mechanisms of the observed phenomena (Vannucchi et al.,

124 2012; Emergeo Working Group, 2013; Facciorusso et al., 2014; Papathanassiou et al., 2015;

125 Chini et al., 2015; Caputo et al., 2015).

126 The geomorphological features of the studied area are sculptured into the alluvial plain formed

127 by the digressions of a riverbed (Reno river), whose course was continuously changed by man in

128 the past centuries with the aim to control its disastrous floods (Bondesan, 1990; 2001). The

129 original river course was definitely abandoned in the 18th century, so the area where the San

130 Carlo village lies is characterized by the old riverbed and earthen embankments degrading

131 toward the alluvial plain (Fig. 2a,b). Due to the past river digressions, the sediments are

132 characterized by a complex succession of alluvial deposits belonging to the depositional

133 environments of river channel, river embankment, river rout and floodplain.

134   The local Emilia-Romagna stratigraphic sequence is divided into an upper and a lower sub-

135   sequence. The upper sub-sequence is divided into 8 members, whose youngest two characterize

136   the local stratigraphical succession of the studied area. The Holocene deposits are approximately

137   20 m thick and formed by sandy-silty deposits of river channel, river embankment, river rout

138   and by clayey-silty deposits of floodplain with frequent lateral heterogeneities. The upper

139   Pleistocene deposits follow beneath with an approximate thickness of 60 m, formed by a

140   multilayering of fine sediments of marsh origin and coarser sediments of river overflowing.

141   The complex soil layering does not allow an easy reconstruction of the lithological succession,

142   characterized by frequent lateral and vertical variations (Romeo et al., 2015). Due to the

143   complex soil layering, the hydrogeological features are also complex since the ground water

144   table, oscillating within the first 10 m depth, is hosted in a multilayer aquifer. Although there is

145   a correlation between the ground slope and the direction of drainage, their different gradients

146   imply that the ground water depth is maximum below the old riverbed and progressively

147   decreases toward the floodplain, thus implying different stress conditions in the subsoil. A

148   monitoring period of two years, whose data are available thanks to the Emilia region technical

149   offices, highlights that the ground water table oscillations are limited to less than 2 meters, with

150   a shallower depth during the spring and the deepest one at the end of the summer season.

151   The area is studied by extensive field investigations mainly consisting of penetrometer tests,

152   integrated by boreholes and some dilatometer tests available in several reports and already

153   collected by Papathanassiou et al. (2015). More in particular, the Liquefaction Potential Index

154   (LPI) and Liquefaction Severity Number (LSN) indexes (Iwasaki et al., 1978; Toprak and

155   Holzer, 2003) have been demonstrated to be suitable for detecting the tendency of different

156   subsoil conditions to generate, or not, liquefaction surface manifestations (Giannakogiorgios et

157   al., 2015). As reported in Papathanassiou et al. (2015), both LSN and LPI allow the

158   identification of local liquefaction-prone conditions at San Carlo when compared to the

159   observed liquefaction effects induced by the 2012 Emilia earthquake (Fig.1a, Table 1). Along

160   the here considered geological cross section (Fig.2b), the resulting LPI values vary from 11.2 up

161   to 25.7 while the LSN values range from 8.2 up to 27.6. According to Papathanassiou et al.

162   (2015), the so resulting correlation classes vary from 3 to 4, identifying a proneness to soil

163   liquefaction from "likely" to "very likely".

164   On the basis of the available investigations, a geological model of the investigated site is

165   reconstructed (Romeo et al., 2015). Fig. 2c shows a NW-SE geological profile across the San

166   Carlo village running parallel to the old river bed. As many investigations refer to indirect

167   geotechnical tests (cone penetration test and dilatometer test), they have been interpreted with

168   the perspective of highlighting the soil layers susceptible to liquefaction. In the case of

169   penetrometer tests, the soil classification by Robertson (1986, 1990) is adopted, as it has been

170   found to be most consistent with the liquefaction susceptibility. Having sampled the sands

171   ejected during the liquefaction effects, their grain size distribution has been used to identify the

172   Robertson's classes indicating liquefaction susceptibility. More in particular, according to

173   Robertson (1986; 1990), classes 7-8-9 are obtained for liquefiable soils, based on CPTU, and 5-

174   6 based on SCPTU; classes 1-2-3-4-5-6-10 are obtained for not liquefiable soils, based on

175   CPTU, and 1-2-3-4-7-8-9 based on SCPTU. The layers susceptible to liquefaction correspond to

176   the grain size classes of sands, silty sands and sandy silt. Based on this classification, the layers

177   belonging to the liquefiable classes are grouped by depth. Due to the stratigraphic succession of

178   liquefiable soil layers and the resulting confining pressures, we can infer that only the first two

179   surficial layers could have been involved in liquefaction phenomena. The geological model

180   highlights that three different columns could represent the local typical layering: 1) a single-

181   layer of surficial liquefiable soils; 2) a double-layer of thin liquefiable soils; 3) a double-layer

182   with one thick and one thin liquefiable soils.

183   The local log-stratigraphy pointed out that within the first 15 meters below the ground, there are

184   one or two layers of liquefiable soils dating to Holocene and representing soils of river

185   embankment and river rout (Fig. 2c). Another layer of liquefiable soils dating back to

186   Pleistocene is present at depths greater than 20 m below the ground (Fig. 2c). Except for the first

187   surficial layer, the other layers are partially or fully confined by non-liquefiable soils (clays and

188   silty clays).

189   According to the aforementioned cross section, it can be derived that two sandy-silty layers

190   (hereafter named LS1 and LS2 respectively) are present in the San Carlo village area within the

191   first 20 m below the ground level. The first layer (LS1) is a superficial deposit with a thickness

192   varying from about 5 up to 10 m and corresponds partly to the recent alluvial deposits of the

193   Reno River and its tributaries, and partly to the old river banks. The thickness of the second,

194   deeper layer (LS2) is variable and ranges between 1 and 7 m, and this layer can be attributed to

195   more ancient alluvial deposits. More in particular, LS1 level is a continuous layer prone to

196   liquefaction whose thickness has a significant variation due to the topographic irregularities,

197   which can be mainly related to the paleo-morphology of the old river banks. Moreover, due to

198   its stratigraphic location, after the seismic shaking, this layer could dissipate the originated pore

199   water overpressures only from the topographic surface. LS2 level is a more discontinuous layer,

200   whose thickness varies within a few meter range, i.e. probably related to floods from ancient

201   river banks. This level shows a not continuous shape along the transversal sections and, where

202   present, it is separated from the LS1 level by a level not susceptible to liquefaction, having a

203 thickness varying up to about 6 m. Due to such a stratigraphic setting, the LS2 level can be

204 regarded as a not drained one, i.e. co-seismic drainage of pore water due to overpressures is not

205 possible. Below the LS2 level an about 10 m thick level not susceptible to liquefaction exists,

206 ascribable to the Pleistocene-Holocene; this level rests above a 5 m thick sandy-gravel level (at

207 about -5 m a.s.l., i.e. 20 m b.g.l.), ascribable to the Pleistocene deposits.

208 Based on the engineering-geological model obtained for the San Carlo village three reference

209 soil columns (C1, C2 and C3 of Fig. 2c) were derived for the 1D numerical modeling, which are

210 summarized below:

211 -   column C1: sandy-silt LS1 and LS2 levels (prone to cyclic mobility and liquefaction) are

212   interlayered with two silty-clayey levels (not susceptible to cyclic mobility and liquefaction)

213   which rest above a sandy-gravel level at about 20 m b.g.l.. This column was obtained by

214   attributing to the silty-clayey level between LS1 and LS2 the lowest assumable thickness

215   (i.e. equal to 2.3 m).

216 -   column C2: sandy-silt LS1 and LS2 levels (prone to cyclic mobility and liquefaction) are

217   interlayered with two silty-clayey levels (not susceptible to cyclic mobility and liquefaction)

218   which rest above a sandy-gravel level at about 20 m b.g.l.. This column was obtained by

219   attributing to the silty-clayey level between LS1 and LS2 the highest assumable thickness

220   (i.e. equal to 5.2 m).

221 -   column C3: a unique sandy-silt LS1+LS2 level prone to liquefaction is considered with the

222   highest assumable thickness (i.e. equal to 12 m).

223 The safety factor (SF) against liquefaction has been computed for each column by the code CLiq

224 v1.7 (Geologismiki®) according to the method of Robertson & Wride (1998), based on the ratio

225 of demand (cyclic stress ratio) and capacity (cyclic resistance ratio). Only the sandy layers

226 between 5 and 10 m deep resulted to be liquefiable (SF < 1) in agreement with the results

227 obtained by Facciorusso et al. (2015).

228

229 **ONE-DIRECTIONAL THREE-COMPONENT WAVE PROPAGATION MODEL**

230 The subsoil is assumed as horizontally layered (as it can be confirmed by the vertical section

231 shown in Fig. 2c) and is modeled as a 1D soil profile (Fig. 3), considering its very large lateral

232 extension. The multilayered soil is assumed infinitely extended along the horizontal directions

233 x and y and, consequently, no strain variation is considered in these directions. A three-

234 component seismic wave propagates vertically in z-direction from the top of the underlying

235 elastic bedrock to the free surface. The soil is assumed to be a continuous medium, with

236 nonlinear constitutive behavior.

237 The soil profile is discretized, using a finite element scheme, into quadratic line elements having

238 three translational degrees of freedom per node. The finite element model applied in the present

239 research is completely described in Santisi d'Avila et al. (2012).

240 The subsoil layers are bounded at the bottom by a semi-infinite elastic medium, representing the

241 seismic bedrock. The absorbing boundary condition proposed by Joyner & Chen (1975) is

242 applied at the soil-bedrock interface to take into account the finite rigidity of the bedrock and

243 allows energy to be radiated back into the underlying medium. The bedrock is characterized by

244 the shear and pressure wave velocities in the medium and density. The 3C velocity time histories

245 at the bedrock level are obtained by deconvolution of a seismic signal representative of

246 outcropping bedrock. The soil motion at the soil-bedrock interface, i.e. at the first node of the

247 mesh (Fig. 3), is composed of the incident and reflected waves and it is computed during the

248 process. At this regard, the interested reader can refer to Santisi d'Avila et al. (2012) for more

249   details. As the considered horizontally layered subsoil is bounded at the top by the free surface,

250   the stresses normal to the free surface are assumed to be null.

251   The finite element size in each soil layer is defined as the minimum between 1m and λ/p,

252   where $\lambda = v_{si}/f$, $p = 10$ is the minimum number of nodes per wavelength to accurately

253   represent the seismic signal, v_{si} is the shear wave velocity in the i-th soil layer and $f = 15\,\text{Hz}$ is

254   the maximum frequency above which the spectral content of the input signal can be considered

255   negligible. The number of finite elements per layer takes into account the expected reduction of

256   the shear wave velocity v_s, during the dynamic process, that modifies the wavelength $\lambda = v_{si}/f$.

257   The implicit dynamic process is solved step-by-step by Newmark's algorithm. The two

258   parameters $\beta = 0.3025$ and $\gamma = 0.6$ guarantee an unconditional numerical stability of the time

259   integration scheme (Hughes, 1987) and numerical damping, to reduce the not physical high

260   frequency content numerically generated without having any significant effect on the

261   meaningful, lower frequency response. According to Hughes (1987), the numerical damping is

262   about 3% at 10Hz. Moreover, the nonlinearity of soil demands the linearization of the

263   constitutive relationship within each time step. The discrete dynamic equilibrium equation does

264   not require an iterative solving, within each time step, to correct the tangent stiffness matrix, if a

265   small fixed time step $dt = 10^{-4}\,\text{s}$ is selected. Gravity load is imposed as static initial condition in

266   terms of strain and stress.

267

268   **FEATURES OF THE 3D NONLINEAR HYSTERETIC MODEL**

269   The 3D elasto-plastic model for soils used in the presented finite element scheme is inspired

270   from that suggested by Iwan (1967) and applied by Joyner (1975) and Joyner and Chen (1975) in

271   a finite difference formulation, in terms of total stresses.

272   The adopted model for TSA of soils satisfies the so-called Masing criteria (Kramer, 1996) that

273   does not depend on the number of loading cycles. As a consequence, in a total stress analysis, the

274   effects of the soil nonlinearity could be overestimated reducing the maximum strain values.

275   According to Joyner (1975), the tangent constitutive matrix is deduced from the actual strain

276   level and the strain and stress values at the previous time step. Then, the knowledge of this

277   matrix allows calculating the stress increment. Consequently, the stress level depends on the

278   strain increment and strain history but not on the strain rate. Therefore, this rheological model

279   has no viscous damping. The energy dissipation process is purely hysteretic and does not depend

280   on the frequency.

281   A correction of mechanical properties is applied according to Iai's model (Iai et al., 1990a,b), for

282   liquefiable soil layers. Iai's rheological model for saturated soils allows attaining larger strains

283   with proper accuracy describing the cyclic mobility process. This correction for liquefiable soils

284   results in a reduction of hysteretic damping overestimation due to the Masing criteria and an

285   increase of the expected maximum strains.

286

287   **Plasticity model**

288   Iwan's model is a 3D elasto-plastic model with linear kinematic hardening, that allows taking

289   into account the nonlinear hysteretic behavior of soils. Elastic parameters are the shear modulus

290    $G_0 = \rho v_s^2$ (where ρ is the mass density and v_s the shear wave velocity in the medium) and the P-

291   wave modulus $M = \rho v_p^2$ (where v_p is the pressure wave velocity in the medium). The Poisson's

292   ratio ν is related with the compressional to shear wave velocity ratio as

293    $(v_p / v_s)^2 = 2(1-\nu)/(1-2\nu)$.

294   The 6-dimensional vector of total deviatoric strain rate $\Delta\mathbf{e}$ is written in terms of the elastic and

295   plastic deviatoric strain rates as $\Delta\mathbf{e} = \Delta\mathbf{e}_E + \Delta\mathbf{e}_P$. The elastic deviatoric strain vector is

296    $$\Delta\mathbf{e}_E = \mathbf{S}/(2G_0) \tag{1}$$

297   where $\mathbf{S}$ is the 6-dimensional deviatoric stress vector.

298   The plasticity model uses von Mises yield surfaces that assume a pressure-independent behavior,

299   namely, yielding is independent of the average pressure stress p. This assumption is acceptable

300   for soils in undrained conditions<mark>, as during a sudden seismic event</mark>. However, the Iai's correction

301   for effective stress analysis is pressure-dependent.

302   A family of n yield surfaces is represented by the yield functions

303    $$F_i(\mathbf{S} - \mathbf{\alpha}_i) - \tau_i^2 = 0 \tag{2}$$

304   where $\mathbf{\alpha}_i$ is the kinematic shift of the ith yield surface and $F_i(\mathbf{S} - \mathbf{\alpha}_i)$ is the ith von Mises yield

305   surface defined as

306    $$F_i(\mathbf{S} - \mathbf{\alpha}_i) = 1/2(\mathbf{S} - \mathbf{\alpha}_i)^T (\mathbf{S} - \mathbf{\alpha}_i) \tag{3}$$

307   The size of the yield surface $\tau_i = \tau_i(e_i)$ is imposed by giving the value of the yield shear stress

308   τ_i, as a function of shear strain e_i, in the case of simple shear.

309   The kinematic hardening models are used to simulate the inelastic behavior of materials that are

310   subjected to cyclic loading. The linear kinematic model approximates the hardening behavior

311   with a constant rate of hardening, as expressed by the Prager hardening rule

312    $$\Delta\mathbf{\alpha}_i = C_i \Delta\mathbf{e}_{Pi} \tag{4}$$

313   where C_i are the initial kinematic hardening moduli for each back stress $\mathbf{\alpha}_i$, defined as (Joyner,

314   1975)

315    $$\frac{1}{C_i} = \frac{e_{i+1} - e_i}{\tau_{i+1} - \tau_i} - \frac{1}{2G} - \sum_{j=1}^{i-1} \frac{1}{C_j} \tag{5}$$

316   The plasticity model assumes an associated plastic flow, which allows for isotropic yield.

317   Therefore, as the material yields, the inelastic deformation rate is in the direction of the normal to

318   the yield surface (the plastic deformation is volume invariant). The rate of plastic flow $\Delta\mathbf{e}_P$ is

319   defined by the following flow rule:

320
$$\Delta\mathbf{e}_{Pi} = L_i\,\Delta\lambda_{Pi}\,\frac{\partial F_i}{\partial\mathbf{S}} \tag{6}$$

321   The coefficient L_i is defined as

322
$$L_i = 0 \quad \text{for} \quad F_i < \tau_i^2 \quad \text{or} \quad \frac{\partial F_i}{\partial\mathbf{S}}\,d\mathbf{S} < 0$$
$$L_i = 1 \quad \text{for} \quad F_i = \tau_i^2 \quad \text{and} \quad \frac{\partial F_i}{\partial\mathbf{S}}\,d\mathbf{S} \geq 0 \tag{7}$$

323   and $\Delta\lambda_P$ is the plastic strain rate, that is deduced, according to Fung (1965) as

324
$$\Delta\lambda_{Pi} = \frac{1}{C_i}\frac{\dfrac{\partial F_i}{\partial s_{rs}}\Delta S_{rs}}{\dfrac{\partial F_i}{\partial s_{lm}}\dfrac{\partial F_i}{\partial s_{lm}}} \tag{8}$$

325   Consequently, the terms of the plastic deviatoric strain $\Delta\mathbf{e}_{Pi}$ in equation (6) become

326
$$\Delta e_{Pi\,hj} = \left[\sum_{i=1}^{n} L_i\frac{1}{C_i}\frac{\dfrac{\partial F_i}{\partial S_{rs}}}{\dfrac{\partial F_i}{\partial S_{lm}}\dfrac{\partial F_i}{\partial S_{lm}}}\frac{\partial F_i}{\partial S_{hj}}\right]\Delta S_{rs} \tag{9}$$

327   Writing the incremental constitutive relationship as

328
$$\Delta\mathbf{e} = \mathbf{E}_d^{-1}\,\Delta\mathbf{S} \tag{10}$$

329   and considering equations (1) and (9), the terms of the inverse deviatoric constitutive matrix $\mathbf{E}_d^{-1}$

330   are deduced as

$$331 \qquad \frac{1}{2G_0} + \sum_{i=1}^{n} L_i \frac{1}{C_i} \frac{\dfrac{\partial F_i}{\partial S_{rs}}}{\dfrac{\partial F_i}{\partial S_{lm}} \dfrac{\partial F_i}{\partial S_{lm}}} \frac{\partial F_i}{\partial S_{hj}} \qquad (11)$$

332   Coefficients in equation (11) are the derivatives of functions F_i in equation (3), that are

$$333 \qquad \frac{\partial F_i}{\partial S_{jk}} = \frac{1}{2}\left(S_{jk} - \alpha_{i\,jk}\right) \qquad (12)$$

334   When the deviatoric constitutive matrix is known, it is possible to evaluate the deviatoric stress

335   rate as $\Delta \mathbf{S} = \mathbf{E}_d \,\Delta \mathbf{e}$. The (6×6)-dimensional tangent constitutive matrix $\mathbf{E}$, that relates the total

336   stresses and strains in the form $\Delta \boldsymbol{\sigma} = \mathbf{E}\,\Delta \boldsymbol{\varepsilon}$, is obtained from $\mathbf{E}_d$ according to Santisi d'Avila et

337   al. (2012).

338   According to Joyner (1975), to ensure that the stress remains on the yield surface, $\Delta \boldsymbol{\alpha}_i$ is not

339   calculated using equation (4), but the following relationship:

$$340 \qquad \boldsymbol{\alpha}_{i\,k+1} = \mathbf{S}_{k+1} - \frac{\tau_i \left(\mathbf{S}_{k+1} - \boldsymbol{\alpha}_{ik}\right)}{\sqrt{1/2 \left(\mathbf{S}_{k+1} - \boldsymbol{\alpha}_{ik}\right)^T \left(\mathbf{S}_{k+1} - \boldsymbol{\alpha}_{ik}\right)}} \qquad (13)$$

341   The failure curve $\Delta \tau(\gamma) = G(\gamma)\Delta \gamma$, where $G(\gamma)$ is the shear modulus decay curve versus shear

342   strain γ is needed to characterize the soil behavior. The main feature of Iwan's model is that the

343   mechanical parameters to calibrate the rheological model are easily obtained from laboratory

344   dynamic tests on soil samples.

345   The applied constitutive model does not depend on the selected initial loading curve. In the

346   present study, normalized shear modulus decay curves are provided by laboratory tests, as

347   resonant column (RC), and fitted by the function $G(\gamma)/G_0 = 1/\left(1 + |\gamma/\gamma_{r0}|\right)$, where γ_{r0} is a

348   reference shear strain corresponding to an actual tangent shear modulus $G(\gamma)$ equivalent to 50%

349   of the elastic shear modulus G_0. This model provides a hyperbolic stress-strain curve (Hardin

350   and Drnevich, 1972), having asymptotic shear stress $\tau_0 = G_0 \gamma_{r0}$ in the case of simple shear. If no

351   additional information is available, the normalized compressional modulus reduction curve

352   E/E_0 is assumed equal to the shear modulus reduction curve G/G_0, under the commonly

353   agreed hypothesis of constant Poisson's ratio during the time history.

354

355   **Correction of mechanical parameters for soils in ESA**

356   Effective stresses follow Terzaghi's law. Note that in the presented formulation the prime

357   indicates effective stresses. The average effective stress is defined as

358    $p' = \left(\sigma_1' + \sigma_2' + \sigma_3' \right)/3 = p - u$, where $p = \left(\sigma_1 + \sigma_2 + \sigma_3 \right)/3$ is the average total stress, σ_1, σ_2 and

359   σ_3 are the principal stresses and u is the pore water pressure. The initial average effective stress

360   is p_0'. The deviatoric stress is $\tau = \left(\sigma_{max} - \sigma_{min} \right)/2 = \tau'$, where σ_{max} and σ_{min} are the maximum

361   and minimum principal stresses, respectively.

362   The liquefaction front in the plane (r, S) is represented in Fig. 4, where $S = p'/p_0'$ is the state

363   variable, with $0 \leq S \leq 1$, and $r = \tau/p_0'$ is the deviatoric stress ratio. According to Iai et al.

364   (1990a,b), the state variable S relates the initial and the actual average effective stress and it is

365   expressed as

366
$$S = \begin{cases} S_0 & r \leq r_3 \\ S_2 + \sqrt{\left(S_0 - S_2 \right)^2 + \left[\left(r - r_3 \right)/m_1 \right]^2} & r > r_3 \end{cases} \qquad (14)\text{a,b}$$

367   where $m_1 = \tan \alpha = \sin \phi'$ is the failure line slope (Fig. 4) and ϕ' is the shear friction angle. It can

368   be remarked in Fig. 4 that $\left(r_2 - r_3 \right)/\left(S_0 - S_2 \right) = m_1$. Accordingly, the parameter S_2 is obtained as

369
$$S_2 = S_0 - (r_2 - r_3)/m_1 \qquad (15)$$

370 In equation (15), it is $r_2 = m_2 S_0$, $r_3 = m_3 S_0$, $m_3 = 0.67 m_2$ and $m_2 = \tan \alpha_p = \sin \phi'_p$ is the phase

371 transition line slope (Fig. 4), where ϕ'_p the phase transformation angle.

372 The initial value of liquefaction front parameter S_0 is determined by imposing the initial

373 condition $S = 1$ in equation (14)b, according to (15). In dry and non-liquefiable layers, it is $S = 1$

374 during the seismic event.

375 Iai et al. (1990a,b) provide a relationship to correlate the liquefaction front parameter S_0 and the

376 normalized shear work w, as follows:

377
$$
\begin{aligned}
S_0 &= (0.4 - S_1)(w_1/w)^{p_2} + S_1 \quad && w \geq w_1 \\
S_0 &= 1 - 0.6(w/w_1)^{p_1} && w < w_1, \ S_1 = 1
\end{aligned}
\qquad (16)\text{a,b}
$$

378 Accordingly, it is

379
$$
\begin{aligned}
w &= w_1 \left[(S_0 - S_1)/(0.4 - S_1) \right]^{-1/p_2} && S_0 \leq 0.4 \\
w &= w_1 \left[(1 - S_0)/0.6 \right]^{1/p_1} && S_0 > 0.4
\end{aligned}
\qquad (17)\text{a,b}
$$

380 The normalized shear work is $w = W_s/W_n$. The normalization factor is $W_n = (p'_0 m_1)\gamma_{r0}/2$,

381 where γ_{r0} is the reference strain used in the hyperbolic formulation adopted for the backbone

382 curve. The plastic shear work W_s is unknown at the initial conditions and it is estimated from w

383 (equation (17)) and W_n. The correlation between S_0 and w, in equation (17), depends on four

384 material parameters S_1, w_1, p_1 and p_2 that characterize the liquefaction properties of the

385 cohesionless soil.

386 The main process starts with the computation of the actual plastic shear work. The increment of

387 plastic shear work at each time step is

18

388
$$dW_s = R\left(dW_{st} - c_1 dW_{se}\right) \geq 0 \tag{18}a,b$$

389   where, according to Towhata and Ishihara (1985), the shear stress work dW_{st} is evaluated as

390   difference between the total work $dW = \sigma'_{ij} d\varepsilon_{ij}$ and the consolidation work $dW_c = p' d\varepsilon_v$, where

391     $d\varepsilon_v$ is the volumetric strain. There exists a threshold limit in the amplitude of cyclic shear strain

392   or shear stress. There is no pore water pressure build-up for cyclic strain or stress below this

393   threshold level. The shear work consumed by the threshold limit is subtracted from the total

394   shear work. It is closely related with the elastic shear work $dW_{se} = \left|\tau d\left(\tau/G\right)\right|$. The parameter

395     $c_1 \approx 1$ is introduced to correct the elastic shear work dW_{se} for the purpose of obtaining the shear

396   work consumed by the threshold limit. R is a correction factor for dW_s in the case of dilatancy,

397   that means $\tau > p_0 m_2$, and $r/S > m_3$. It is defined as

398
$$\begin{aligned}
R &= \left(m_1 - r/0.4\right)/\left(m_1 - m_3\right) &\quad S_0 \leq 0.4 \\
R &= \left(m_1 - r/S\right)/\left(m_1 - m_3\right) &\quad S_0 > 0.4
\end{aligned} \tag{19}a,b$$

399   When the actual plastic shear work W_s is known, the normalized shear work w is evaluated, the

400   liquefaction front parameter S_0 is deduced from equation (16) and the state variable S is

401   obtained by equation (14). According to the definition of S, the actual average effective stress

402     $p' = S p'_0$ and the increment of water pressure $\Delta u = p'_0 - p' > 0$ are obtained during the time

403   history. The actual effective stress $\sigma' = \sigma - u$ is deduced from the total stress and water pressure

404     $u = p - p'$. Finally, the updated deviatoric stress τ_a and the reference shear strain γ_{ra} are

405   estimated as

406
$$\begin{aligned}
\tau_a &= \tau_0 S & \gamma_{ra} &= \gamma_{r0} & S_0 &> 0.4 \\
\tau_a &= \tau_0 S + \Delta\tau = \tau_0 S + \tau_0\left(1 - m_1/m_2\right)\left(0.4 - S_0\right) & \gamma_{ra} &= \gamma_{r0}/\left(S_0/0.4\right) & S_0 &< 0.4
\end{aligned} \tag{20}a,b$$

407   The corrected shear modulus is

408
$$G_a = \tau_a / \gamma_{ra} \tag{21}$$

409   Consequently, the normalized shear modulus decay curve is updated as

410    $G(\gamma)/G_a = 1/\left(1+|\gamma/\gamma_{ra}|\right)$.

411

412   **Characterization of soil parameters in ESA**

413   Seven parameters have to be fixed to calibrate Iai's correction of shear modulus of soils for ESA.

414   They are the shear friction angle ϕ', the phase transformation angle ϕ'_p, the parameter c_1 that

415   corrects the elastic shear work and the four parameters S_1, w_1, p_1 and p_2 that influence the

416   relationship between the liquefaction front parameter S_0 and the normalized shear work w.

417   The shear friction angle ϕ' and the phase transformation angle ϕ'_p are obtained from static

418   Consolidated Undrained (CU) triaxial tests, using the (τ, p') curve for three different confining

419   pressure levels. The slope of the line connecting the rupture points, for the three different

420   confining pressure levels, is the trigonometric tangent of angle α. The slope of the line

421   connecting the inflection points of the three curves is the trigonometric tangent of angle α_p. The

422   shear friction angle ϕ' and the phase transformation angle ϕ'_p are obtained considering the

423   equivalences $\tan\alpha = \sin\phi'$ and $\tan\alpha_p = \sin\phi'_p$, respectively.

424   According to Iai et al., 1990a,b, parameters S_1, w_1, p_1 and p_2 are deduced from CTX tests.

425   Three curves have to be reproduced: the cyclic deviatoric stress, the deviatoric strain amplitude

426   and the normalized excess pore water pressure $\Delta u/p'_0$ with respect to the number of cyclic

427   loading N, where $\Delta u = p'_0 - p'$ is the excess pore water pressure.

428

MODEL OF SELECTED SOIL PROFILES

429

430   The definition of the three analyzed soil profiles, named here C1, C2 and C3, is derived from the

431   stratigraphy in the San Carlo area, at about 17 km from the epicenter of the 2012 Emilia

432   earthquake. The selected stratigraphy for the three columns C1, C2 and C3, and the mechanical

433   parameters identified for each layer are presented in Tables 2, 3 and 4, respectively. The front

434   liquefaction parameters are also reported for cohesionless soil layers, subjected to possible

435   cyclic mobility effects and liquefaction phenomena. Liquefiable soil layers are the 1st, 3rd and

436   5th in soil columns C1 and C2, and the 1st and 3rd in C3.

437   An in-situ test using seismic dilatometer has been used to obtain profiles with depth of the shear

438   wave velocity v_s, total (wet) density ρ and at-rest lateral earth pressure coefficient K_0. The

439   initial elastic shear modulus G_0 is evaluated as $G_0 = \rho v_s^2$. The elastic P-wave modulus is

440   evaluated as $M_0 = \rho v_p^2$, where the compressional wave velocity v_p is deduced from the

441   relationship $v_p = v_s \sqrt{2(1-\nu)(1-2\nu)}$, where the Poisson's ratio is obtained as $\nu = K_0/(1+K_0)$.

442   Laboratory tests are used to obtain the mechanical features of each soil layer, useful to define

443   the initial conditions in the numerical simulation. A RC test gives the normalized shear modulus

444   reduction curve $G(\gamma)/G_0$ that is fitted using a curve corresponding to a hyperbolic stress-strain

445   curve. The reference shear strain γ_{r0} is deduced as the strain corresponding to $G = 0.5 G_0$. The

446   shear modulus reduction curves obtained by laboratory data are given in Table 5, for the soil

447   samples used to characterize the analyzed soil columns. The normalized curves, fitted by the

448   hyperbolic model are shown in Fig. 5.

449   The variation of the elastic shear modulus with depth is taken into account for the liquefiable

450   soil layers. It is corrected according to $G_0(z) = G_0(z_m) p_0'(z)/p_0'(z_m)$, where p_0' is the average

451   pressure, z_m is the depth at the middle of the layer and $G_0(z_m) = \rho v_s^2$ is calculated using the

452   values of density and shear velocity reported in Tables 2-4 for each soil layer. As consequence,

453   the shear strength $\tau_0 = G_0 \gamma_{r0}$ is modified. In non-liquefiable layers, considering that their

454   thickness is limited, the shear modulus is assumed constant with depth.

455   A CU triaxial test provides the shear friction angle ϕ' and the phase transformation angle ϕ_p'

456   using a curve (τ, p') for three different confining pressure levels. The slope of the line

457   connecting the rupture points, for the three different confining pressure levels, is the

458   trigonometric tangent of the shear friction angle ϕ'. The slope of the line connecting the

459   inflection points of the three curves is the trigonometric tangent of the phase transformation

460   angle ϕ_p'.

461   The CTX test gives the liquefaction front parameters c_1, S_1, w_1, p_1 and p_2 as explained in the

462   next subsection.

463   The average effective stress in geostatic conditions $p_0' = (\sigma_v' + 2\sigma_h')/3$ is evaluated considering

464   the vertical effective stress $\sigma_v'(z) = \rho g z - u_0(z)$, variable with depth z (g is the gravitational

465   acceleration) and dependent on the initial pore water pressure $u_0(z)$, and the horizontal

466   effective stresses estimated as $\sigma_h'(z) = K_0 \sigma_v'(z)$. At the surface, where the vertical stress attains

467   zero but the confinement, even if reduced, is not annulled, the horizontal effective stresses are

468   corrected and assumed equal to $\sigma_h' = K_0 \sigma_v'(z_p)$ in the first z_p meters (in this study, it is

469   assumed $z_p = 5\,\mathrm{m}$).

470

471   **Fitting of cyclic consolidated undrained triaxial test curves**

472   The parameters S_1, w_1, p_1 and p_2 are deduced from CTX tests. The cyclic deviatoric stress

473   (total axial stress minus confining pressure) produced during the test is used to estimate the total

474   axial stress that is adopted as input in a numerical simulation, known the cell pressure

475     $p_0 = 300\,\text{kN}/\text{m}^2$ and the back pressure $u_0 = 200\,\text{kN}/\text{m}^2$ during the test. The axial deviatoric

476   strain amplitude and the normalized excess pore water pressure $\Delta u/p_0'$ ($\Delta u = p_0' - p'$ is the

477   excess pore water pressure), with respect to the number of cyclic loading N, are obtained

478   numerically and compared to the two curves produced during the test.

479   In order to obtain numerically the curves that best reproduce the experimental ones, the

480   parameters w_1 and p_1 are determined by a trial-and-error procedure, to obtain a normalized

481   excess pore water pressure curve that best reproduce the experimental curve in the portion of the

482   curve for $\Delta u/p_0' < 0.6$. The parameter w_1 is not greatly influenced by the variation of p_1, so it is

483   determined at first for a given value of p_1. The appropriate value of p_1 is researched in the

484   interval $[0.4 - 0.7]$, according to Iai et al. (1990b). The greater w_1 and p_1 are, the slower the

485   pore water pressure rises. The envelope of strain amplitude is also fitted, observing that the

486   greater w_1 is, the more it reduces the envelope of strain amplitude.

487   The parameter p_2 is researched in the interval $[0.6 - 1.5]$ (Iai et al. 1990b). It is determined as

488   well by a trial-and-error process, to obtain a normalized excess pore water pressure curve that

489   best fit the experimental curve in the portion of the curve for $\Delta u/p_0' > 0.6$. Since the curve is not

490   greatly influenced by the variation of p_2, the envelope of strain amplitude is also fitted. The

491   greater p_2 is, the more it increases the envelope of strain amplitude.

492   According to Iai et al. (1990b), the parameter $S_1 \geq 0.005$ is introduced so that S_0 will never be

493   zero. It takes small positive values, determined by the trial-and-error procedure to obtain the best

494   fit of the experimental normalized excess pore water pressure curve. The analyzed tests appear

495   not sensitive to a variation of S_1. The first trial is maintained for all the layers: $S_1 = 0.005$. The

496   parameter c_1 is imposed equal to one when w_1, p_1 and p_2 are determined and, if laboratory data

497   are not well represented in the elastic range, c_1 can be modified using a trial-and-error procedure.

498   The mechanical parameters measured by laboratory tests (RC, CU) are listed in Table 6 for the

499   analyzed soil samples S11-C1 (associated to the liquefiable layer LS1 in Tables 2-4) and S11-C3

500   (associated to LS2). The selected liquefaction parameters for S11-C1 and S11-C3 are the average

501   between the values obtained by calibration for the two available tests (listed in Table 6) and these

502   selected values are assumed constant with depth within each liquefiable soil layer. The fitting of

503   CTX test curves is shown in Fig. 6 for the S11-C1-2 soil sample (see Table 6) and in Fig. 7 for

504   the S11-C1-3 soil sample. Figs 6 and 7 show the measured cyclic axial deviatoric stress, applied

505   as input, the measured and numerical axial deviatoric strain amplitude and normalized excess

506   pore water pressure with respect to the number of cyclic loading. The curves (τ, p') and (r, S)

507   are evaluated numerically.

508

509   **Input seismic motion**

510   Since in May 2012 the stations of the fixed Italian National Accelerometric Network (RAN)

511   were not present in the municipal area of San Carlo, the mainshock was not recorded in this site.

512   Even though the temporary array, installed the day after the mainshock by the Nacional Civil

513   Protection, recorded 12 seismic events with M_w higher than 4, no further liquefaction effects

514   have been observed after the mainshock of 20 May 2012. Therefore, as reported by Romeo et al.

515 (2015), the seismic input at the San Carlo site was derived by: 1) evaluating a spectrum of

516 scenario for the site of San Carlo; 2) selecting the record of the 20 May 2012 mainshock at

517 Mirandola as reference input and deconvolving it to bedrock and outcrop; 3) attenuating the

518 record of Mirandola at the outcropping bedrock of San Carlo using the ground motion prediction

519 equation proposed by Sabetta and Pugliese (1987).

520 The three-components of the reference outcropping motion are halved and applied as incident

521 wavefield at the base of the analyzed soil columns.

522 The reference incident motion applied at the soil-bedrock interface is shown in Fig. 8, in terms of

523 acceleration. The peak acceleration is 2.54 m/s^2 in North-South direction (named x in the

524 model), 1.51 m/s^2 in East-West direction (named y) and 0.33 m/s^2 in Up-Down direction

525 (named z).

526 All input and output signals are filtered using a 4-pole Butterworth bandpass filter in the

527 frequency range $0.1-15\,Hz$.

528

529 **EEFECT OF WATER TABLE DEPTH VARIATION**

530 First, the seismic response of the analyzed soil profiles to the 20 May 2012 Mw 5.9 Emilia

531 earthquake is estimated in terms of total stresses, to assess the extent of error in this study case

532 where liquefaction phenomena are expected. Then, the analysis is developed in terms of effective

533 stresses.

534 The assumed water table depth is $z_w = 5.8\,m$ for C1 column, $z_w = 5.2\,m$ for C2 column and

535 $z_w = 2.7\,m$ for C3 column, according to the available technical reports. Moreover, a water table

536 variation of $\pm 1m$ is considered in this research and its influence on the soil column response to

537 the seismic loading is analyzed.

538   Profiles with depth of the peak acceleration and velocity, shear strain and stress for the soil

539   profile C1 are represented in Fig. 9, in the cases of TSA and ESA with variable water table

540   position. Strains are increased in liquefiable layers, compared with the TSA assumption. The

541   shape of loops in liquefiable soil layers is influenced by the reduction of shear modulus during

542   the cyclic mobility (Fig. 10 bottom). Profiles with depth and hysteresis loops for soil columns C2

543   and C3 are presented in Figs 11-12 and 13-14, respectively.

544   In liquefiable soil layers, the shear modulus is reduced during the cyclic mobility and the

545   reference shear strain γ_{r0} is numerically corrected when the liquefaction front parameter S_0 is

546   lower than 0.4, according to Equation (20). The minimum values attained by the shear modulus

547   during the process, at each depth, and the maximum reference shear strain are shown in Fig. 15,

548   for the C3 soil profile.

549   Observing Figs 9-14, the considered variation of the water table position equal to ± 1m is not

550   influent in the seismic response of the analyzed soil profiles. In the analyzed case study, a total

551   stress analysis, for a stratigraphy where there are liquefiable soil layers, totally modifies the

552   seismic response, neglecting the reduction of soil stiffness and the increase of ground motion.

553   According to Figs 9, 11, 13, 16 and 17 and Table 7, the TSA assumption underestimates the peak

554   values of motion.

555   According to Figs 9, 11 and 13, the maximum shear strain level, estimated using the analysis in

556   terms of effective stress, is 6.8% , 5.6% and 6.2% for C1, C2 and C3 soil profiles, respectively.

557   Maximum acceleration profiles with depth are obtained during the process using unfiltered

558   acceleration. Figs 16-17 show filtered horizontal acceleration at the ground surface. The

559   variability in the peak ground acceleration with the water table position is negligible (see Table

560   7).

561 The expected level of horizontal peak ground acceleration, corresponding to about $0.32\,g$

562 according to the automated shakemaps (INGV, see Data and Resources), is numerically obtained

563 for the C3 soil profile (Table 7).

564 Fig. 18a shows the profiles with depth of maximum excess pore water pressure, normalized with

565 respect to the initial average effective pressure, for the three analyzed soil columns. The

566 maximum excess pore water pressure attains 84%, 93% and 98% of the initial average

567 effective pressure, respectively. The time history at the depth where the excess pore water

568 pressure attains the maximum value is shown in Fig. 18b.

569

570 **CONCLUSIONS**

571 A one-directional propagation model of a three-component seismic wave (1D-3C approach), in a

572 finite element scheme, is used to investigate the seismic response and stress-strain induced

573 effects of three soil profiles derived from the stratigraphy of San Carlo village (Emilia Romagna,

574 Italy). A representative record for the 20 May 2012 Mw 5.9 Emilia earthquake is applied as input

575 motion at the soil-bedrock interface.

576 During the 20 May 2012 Mw 5.9 Emilia earthquake, liquefaction phenomena have been

577 observed. Consequently, an analysis in terms of total stresses is not suitable. A constitutive

578 behavior based on soil plasticity with hardening (Iwan's model) is used, where the nonlinearity is

579 described by the normalized shear modulus reduction curve. The shear modulus is corrected

580 during the process, depending on the actual average effective stress (Iai's model) to consider the

581 cyclic mobility and dilatancy of sands.

582 The seismic response of the analyzed soil profiles is discussed in terms of profiles with depth of

583 maximum shear strain and stress, peak of the horizontal motion and maximum excess pore water

584   pressure. Hysteresis loops in liquefiable soils and the time histories of the ground motion and the

585   excess pore water pressure are obtained for the different hypothesis of the water table depth.

586   The impact of ESA soil modeling in the numerical seismic response of a soil profile, compared

587   with a total stress analysis, is observed for the analyzed case study and shows that the TSA

588   assumption underestimates the peak values of the ground motion.

589   The influence on the numerical seismic response and the stress-strain effects of the water table

590   depth variability is investigated and it appears negligible in the analyzed case study.

591   The attained maximum shear strain level, estimated using nonlinear analysis in terms of effective

592   stress, attains 6%, confirming the observed liquefaction effect. The expected level of horizontal

593   peak ground acceleration, deduced from the automated shakemaps, is numerically reproduced.

594   The maximum excess pore water pressure, obtained numerically, attains 98% of the initial

595   average effective pressure in C3 soil profile.

596   The discrepancy between geotechnical parameters, obtained by different in-situ and laboratory

597   tests, forces to some modeling choices. Further experimental research should be necessary to

598   guarantee the interdependence of geotechnical data issued by tests for different soil samples in

599   the same area and to regulate the procedure allowing the transposition of measures in the

600   modeled soil profile.

601   The numerical approach applied here can be regarded as a useful tool for identifying subsoil

602   portion prone to soil liquefaction during earthquakes. This allows the outline of unstable zones

603   for expected nonlinear effects in the framework of Seismic Microzonazion Studies. In this

604   regard, high resolution engineering-geological modeling of the subsoil makes it possible to

605   extend the local numerical results (i.e. output from a single soil column) to adjacent areas, based

606   on the similarity of soil layering and hydrogeological conditions. Such an approach exemplifies

607 the efficiency of a multidisciplinary approach which merges geological, physical and engineer

608 features to quantify complex effects involving a multiphase rheological system.

609

610 **DATA AND RESOURCES**

611 Seismograms and soil stratigraphic setting used in this study were obtained in the framework of

612 the Project S_2-2012 by INGV-DPC 2012-2013 – UR4 titled: "Validation of Seismic Hazard

613 through observed data; Constraining OBservations into Seismic hazard (COBAS)" (scientific

614 responsible: Laura Peruzza; UR4 co-ordinator R.W. Romeo). The laboratory tests used for this

615 study were performed on commission by the C.G.G. Testing S.r.l. laboratory of Bologna (Italy).

616 The Italian catalogue of earthquake-induced ground effects (CEDIT) is available online at the

617 URL http://www.ceri.uniroma1.it/index_cedit.html (last accessed November 2017).

618 Shakemaps produced by the Italian National Institute of Geophysics and Volcanology (INGV)

619 are available online at the URL http://shakemap.rm.ingv.it/shake/index.html (last accessed

620 November 2017).

621

626

627 **REFERENCES**

628 Bonilla, L.F., R.J. Archuleta and D. Lavallée (2005). Hysteretic and dilatant behavior of

629 cohesionless soils and their effects on nonlinear site response: field data observations and

29

630   modeling, *Bull. Seism. Soc. Am.*, 95(6), 2373–2395.

631   Bondesan, M. (1990). L'area deltizia padana: caratteri geografici e geomorfologici, *Il Parco del*

632   *Delta del Po, studi e immagini*, vol. 1, L'ambiente come risorsa, Spazio Libri Editori, Ferrara,

633   10–48.

634   Bondesan, M. (2001). L'evoluzione idrografica e ambientale della pianura ferrarese negli ultimi

635   3000 anni, *Storia di Ferrara*, vol. 1, Territorio e preistoria, Corbo Editori, Ferrara, 228–263.

636   Caputo, R., A. Pellegrinelli, C. Bignami, A. Bondesane, A. Mantovani, S. Stramondo and P.

637   Russo (2015). High-precision levelling, DInSAR and geomorphological effects in the Emilia

638   2012 epicentral area, *Geomorphology*, **235**, 106–117.

639   Chini, M., M. Albano, M. Saroli, L. Pulvirenti, M. Moro, C. Bignami, E. Falcucci, S. Gori, G.

640   Modoni, N. Pierdicca and S. Stramondo (2015). Coseismic liquefaction phenomenon analysis by

641   COSMO-SkyMed: 2012 Emilia (Italy) earthquake. *Int. J. Appl. Earth Obs. Geoinf.*, **39**, 1–14.

642   Chung, J.W., and J.D. Rogers (2013). Influence of Assumed Groundwater Depth on Mapping

643   Liquefaction Potential. *Environmental & Engineering Geoscience*, **19**(4), 377–389.

644   DPC-CRP - Dipartimento della Protezione Civile e Conferenza delle Regioni e delle Province

645   Autonome (2008). Indirizzi e Criteri per la Microzonazione Sismica; Dipartimento della

646   Protezione Civile: Rome, Italy. http://www.protezionecivile.gov.it/jcms/it/view_pub.wp?content

647   Id=PUB1137.

648   Emergeo Working Group (2012). Liquefaction phenomena associated with the Emilia

649   earthquake sequence of May–June 2012 (Northern Italy). *Nat. Hazards Earth Syst. Sci.*, **13**,

650   935–947.

651   Facciorusso, J., C. Madiai and G. Vannucchi (2014). Soil liquefaction analyses in a test-area

652 affected by the 2012 Emilia-Romagna earthquake (Italy), *Engineering Geology for Society and*

653 *Territory*, vol. 5, Springer, 1111–1114.

654 Facciorusso, J., C. Madiai and G. Vannucchi (2015). CPT-based liquefaction case history from

655 the 2012 Emilia earthquake in Italy, *J. Geotech. Geoenviron. Eng.*, **141**(12), 1032–1051.

656 Fung, Y. C. (1965). *Foundation of soil mechanics*, Prentice Hall, Englewood Cliffs, New Jersey.

657 Giannakogiorgos, A., G.Papathanassiou and E. Vautherin (2015). Quantitative assessment of

658 liquefaction potential in selected areas in Christchurch, New Zealand. Proc. 6th International

659 Conference on Earthquake Geotechnical Engineering 1-4 November 2015 Christchurch, New

660 Zealand, 1-8.

661 Hardin, B.O., and V.P. Drnevich (1972). Shear modulus and damping in soil: design equations

662 and curves, *J. Soil Mech. Found. Div.*, **98**, 667–692.

663 Hartantyo, E., S.K., Brotopuspito, Sismanto, Waluyo (2014). Correlation of shallow

664 groundwater levels with the liquefaction occurrence cause by May 2006 earthquake in the south

665 volcanic-clastic sediments Yogyakarta, Indonesia. *Int. J. of Applied Sciences*, **5**(1), 1–8.

666 Hughes, T.J.R. (1987). *The finite element method - Linear static and dynamic finite element*

667 *analysis*, Prentice Hall, Englewood Cliffs, New Jersey.

668 Iai, S., Y. Matsunaga and T. Kameoka (1990a). *Parameter identification for a cyclic mobility*

669 *mode*, Report of the Port and harbour Research Institute, **29**(4), 27–56.

670 Iai, S., Y. Matsunaga and T. Kameoka (1990b). *Strain space plasticity model for cyclic mobility*,

671 Report of the Port and harbour Research Institute, **29**(4), 57–83.

672 Iwan, W.D. (1967). On a class of models for the yielding behavior of continuous and composite

673 systems, *J. Appl. Mech.*, **34**, 612–617.

674 Iwasaki, T., F. Tatsuoka, K.I. Tokia and S. Yasuda (1978). A practical method for assessing soil

675 liquefaction potential based on case studies at various sites in Japan. 2nd Int. Conf. on

676 Microzonation, San Francisco, Proceedings, pp. 885–896.

677 Nishiwaki, K., Yasuhara, K., Komine, H. and S. Murakami (2009). Displacement and

678 countermeasures for existing structure with rising groundwater levels, Proc. 8th Japan National

679 Symposium on Environmental Geotechnology, pp. 381–384 (Japanese).

680 Joyner, W. (1975). A method for calculating nonlinear seismic response in two dimensions,

681 *Bull. Seism. Soc. Am.*, **65**(5), 1337–1357.

682 Joyner, W.B., and A.T.F. Chen (1975). Calculation of nonlinear ground response in earthquakes,

683 *Bull. Seism. Soc. Am.*, **65**(5), 1315–1336.

684 Kramer, S.L. (1996). *Geotechnical earthquake engineering*, Prentice Hall, New Jersey.

685 Martino, S., A. Prestininzi and R.W. Romeo (2014). Earthquake-induced ground failures in Italy

686 from a reviewed database. *Nat. Hazards Earth Syst. Sci.*, **14**, 799–1814.

687 Papathanassiou, G., A. Mantovani, G. Tarabusi, D. Rapti and R. Caputo (2015). Assessment of

688 liquefaction potential for two liquefaction prone areas considering the May 20, 2012 Emilia

689 (Italy) earthquake, *Engineering Geology*, **189**, 1–16.

690 Régnier, J. *et al.*, 2018. PRENOLIN: international benchmark on 1D nonlinear site response

691 analysis - Validation phase exercise. *Bull. Seism. Soc. Am.*, 108(2).

692 Robertson, P.K., and C.E. Wride (1998). Evaluating cyclic liquefaction potential using the cone

693 penetration test, *Can. Geotech. J.,* **35**, 442–459.

694 Robertson, P.K. (1986). In situ testing and its application to foundation engineering, *Can.*

695 *Geotech. J.,* **23**, 573–594.

696 Robertson, P.K. (1990). Soil classification using the cone penetration test, *Can. Geotech. J.*,

697 **27**(1), 151–158.

698 Romeo, R.W., S. Amoroso, J. Facciorusso, L. Lenti, C. Madiai, S. Martino, P. Monaco, D.

699 Rinaldis and F. Totani (2015). Soil liquefaction during the Emilia, 2012 seismic sequence:

700 investigation and analysis, In G. Lollino et al. (eds.), Engineering Geology for Society and

701 Territory, vol.5, 1107-1110.

702 Sabetta, F., and A. Pugliese (1987). Attenuation of peak horizontal acceleration and velocity

703 from Italian strong-motion records. *Bull. Seism. Soc. Am.*, **77**, 1491–1513.

704 Santisi d'Avila, M.P., L. Lenti, and J.F. Semblat (2012). Modeling strong seismic ground

705 motion: 3D loading path vs wavefield polarization, *Geophys. J. Int.*, **190**, 1607–1624.

706 Santisi d'Avila, M.P., Viet Anh Pham, L. Lenti, J.F. Semblat (2018). Extended Iwan-Iai

707 constitutive model for 1-Directional 3-Component seismic waves in liquefiable soils: application

708 to the Kushiro site (Japan), *Geophys. J. Int.*, in press.

709 Scognamiglio, L., L. Margheriti, F.M. Mele, E. Tinti, A. Bono, P. De Gori, V. Lauciani, F.P.

710 Lucente, A.G. Mandiello, C. Marcocci, S. Mazza, S. Pintore and M. Quintiliani (2012). The

711 2012 Pianura Padana Emiliana seimic sequence: locations, moment tensors and magnitudes,

712 *Annals of Geophysics*, **55**(4), 549–559.

713 Toprak, S., and T.L. Holzer (2003). Liquefaction potential index: field assessment. *J. Geotech.*

714 *Geoenviron. Eng.*, **129** (4), 315–322.

715 Towhata, I., and Ishihara K. (1985). Shear work and pore water pressure in undrained shear.

716 *Soils and foundations*, **25**(3), 73–84.

717 Vannucchi, G., T. Crespellani, J. Facciorusso, A. Ghinelli, C. Madiai, A. Puliti and S. Renzi

718 (2012). Soil liquefaction phenomena observed in recent seismic events in Emilia-Romagna

719   Region (Italy), *Ingegneria sismica*, vol. 2–3, Pàtron Editore, Bologna.

720   Yasuda, S., and K. Ishikawa (2015). Effect of lowering the ground water table as the

721   countermeasure against liquefaction-induced damage to houses. Journal of Japan Association for

722   Earthquake Engineering, **15**(7), 205-219.

723   Wang, C.Y., D.S Dreger, Wang C.H., Mayeri D. and J.G. Berryman (2003). Field relations

724   among coseismic ground motion, water level change and liquefaction for the 1999 Chi-Chi

725   (Mw=7.5) earthquake, Taiwan. *Geophysical Research Letters*, **30**(17), HLS1-4.

726   Wayne, A.C., and D. O. Doehring (2007). Groundwater table mounding, pore pressure, and

727   liquefaction induced by explosions: energy-distance relations. *Reviews of Geophysics*, **45**,

728   RG4006/2007, 1 of 9. Paper number 2006RG000205.

729

35

753   parameters, for S11-C1-2 soil sample in LS1 liquefiable soil layer.

754   **Figure 7.** Fitting of cyclic Consolidated Undrained triaxial test curves to calibrate liquefaction

755   parameters, for S11-C3-3 soil sample in LS2 liquefiable soil layer.

756   **Figure 8.** Three components of the incident motion applied at the soil-bedrock interface in terms

757   of acceleration. The peak acceleration is 2.54 m/s^2 in x -direction, 1.51 m/s^2 in y-direction and

758   0.33 m/s^2 in z-direction.

759   **Figure 9.** Profiles with depth of maximum shear strain and stress, horizontal velocity and

760   acceleration, during the seismic event, for different water table depth and for TSA conditions in

761   the C1 soil column. The horizontal dashed lines indicate the depth where the shear stress-strain

762   loops are analyzed.

763   **Figure 10.** Hysteresis loops in C1 soil profile for different water table depth and for TSA

764   conditions: (top) at 21.5 m in a non liquefiable soil layer; (bottom) at 13 m in LS2 liquefiable

765   soil layer.

766   **Figure 11.** Profiles with depth of maximum shear strain and stress, horizontal velocity and

767   acceleration, during the seismic event, for different water table depth and for TSA conditions in

768   the C2 soil column. The horizontal dashed lines indicate the depth where the shear stress-strain

769   loops are analyzed.

770   **Figure 12.** Hysteresis loops in C2 soil profile for different water table depth and for TSA

771   conditions: at 9 m (top) and at 12.5 m (bottom) in LS2 liquefiable soil layer.

772   **Figure 13.** Profiles with depth of maximum shear strain and stress, horizontal velocity and

773   acceleration, during the seismic event, for different water table depth and for TSA conditions in

774   the C3 soil column. The horizontal dashed lines indicate the depth where the shear stress-strain

775   loops are analyzed.

776   **Figure 14.** Hysteresis loops in C3 soil profile for different water table depth and for TSA

777   conditions: (top) at 20.5 m in a non liquefiable soil layer; (bottom) at 12 m in LS1+LS2

778   liquefiable soil layer.

779   **Figure 15.** Profile with depth of minimum shear modulus (left), during the seismic event, with

780   zoom in the first soil layers (middle) and profile with depth of the maximum reference shear

781   strain, for different water table depth and for TSA conditions, in the C3 soil profile. The

782   horizontal dashed lines indicate the depth where the shear stress-strain loops are analyzed.

783   **Figure 16.** Acceleration time history at the ground surface for C1 (left), C2 (middle) and C3

784   (right) soil profiles, in x-direction, for different water table depth and for TSA conditions.

785   **Figure 17.** Acceleration time history at the ground surface for C1 (left), C2 (middle) and C3

786   (right) soil profiles, in y-direction, for different water table depth and for TSA conditions.

787   **Figure 18.** Excess pore water pressure, normalized with respect to the average effective pressure,

788   for different water table depth, in C1 (left), C2 (middle) and C3 (right) soil columns: (top)

789   Profiles with depth of maximum value during the seismic event. The horizontal dashed lines

790   indicate the depth where the time histories are analyzed. (bottom) Time history: at 21.5 m (LS1)

791   in C1 soil profile, at 20.5 m (LS2) in C2 soil profile and at 4.5 m (LS1+LS2) in C3 soil profile,

792   for $z_w = 3.7\,\mathrm{m}$, at 3.5 m for $z_w = 2.7\,\mathrm{m}$ and $z_w = 1.7\,\mathrm{m}$.

793

794 **AUTHORS' AFFILIATION**

795 Maria Paola Santisi d'Avila

796 Université Côte d'Azur

797 Laboratoire Jean Alexandre Dieudonné (LJAD)

798 28 Avenue Valrose, 06108 Nice, France

799 msantisi@unice.fr

800

801 Salvatore Martino

802 Università Roma "Sapienza"

803 Dipartimento di Scienze della Terra e Centro di Ricerca per i Rischi geologici (CERI)

804 Piazzale Aldo Moro, 5, 00185 Roma, Italy

805 salvatore.martino@uniroma1.it

806

807 Luca Lenti

808 IFSTTAR, Université Paris-Est

809 14-20 Boulevard Newton, 77447 Champs sur Marne, France

810 luca.lenti@ifsttar.fr

811

812 Roberto Walter Romeo

813 Libera Università di Urbino Carlo Bo

814 Via Aurelio Saffi, 2, 61029 Urbino, Italy

815 roberto.romeo@uniurb.it

816

817

TABLES

819   **Table 1.** Values of LPI and LSN referred to the SCPTU and CPTU tests located in Fig. 2a and

820   related correlation classes for proneness to soil liquefaction according to Papathanassiou et al.,

821   2015: class-I: "almost no", class-II: "few", class-III: "likely" and class-IV: "very likely".

In-situ test position	LPI	LSN	Correlation class
SCPTU1	25.7	25.4	4
CPTU2	18.1	16.6	4
CPTU1	12.2	9.0	3
SCPTU3	15.9	15.6	4
CPTU3	15.1	13.5	4
CPTU4	11.2	8.2	3
SCPTU2	25.7	27.6	4

822

823   **Table 2.** Stratigraphy and geotechnical parameters of soil profile C1. The liquefiable layers are

824   referred as LS.

layer	soil type	depth m	density kg/m^3	S-wave velocity m/s	P-wave velocity m/s	earth press. coeff.	reference strain ‰	soil sample
1	sandy silt (LS1)	9.7	1750	185	1234	0.96	0.39	S11-C1
2	silty clay	12.0	1800	180	465	0.7	0.48	
3	sandy silt (LS2)	14.0	1850	180	402	0.6	0.39	S11-C3
4	silty clay	21.5	1800	200	632	0.8	0.48	
5	sandy gravel	27.5	1850	275	710	0.7	0.39	S11-C3
6	silty clay	33.0	1900	280	723	0.7	0.49	
7	sandy gravel	73.0	1975	385	994	0.7	100	
8	silty clay	113	2125	595	1536	0.7	100	
	bedrock	> 113	2200	700	1807	0.7		

825

826

827 **Table 3.** Stratigraphy and geotechnical parameters of soil profile C2**.** The liquefiable layers are

828 referred as LS.

layer	soil type	depth m	density kg/m^3	S-wave velocity m/s	P-wave velocity m/s	earth press. coeff.	reference strain ‰	soil sample
1	sandy silt (LS1)	3.3	1700	200	894	0.9	0.39	S11-C1
2	silty clay	8.5	1750	190	601	0.8	0.48	
3	sandy silt (LS2)	12.5	1850	200	516	0.7	0.39	S11-C3
4	silty clay	20.5	1850	210	939	0.9	0.48	
5	sandy gravel	26.0	1850	275	710	0.7	0.39	S11-C3
6	silty clay	33.0	1900	280	723	0.7	0.49	
7	sandy gravel	73.0	1975	385	994	0.7	100	
8	silty clay	113	2125	595	1536	0.7	100	
	bedrock	> 113	2200	700	1807	0.7		

829

830 **Table 4.** Stratigraphy and geotechnical parameters of soil profile C3. The liquefiable layers are

831 referred as LS.

layer	Soil Type	depth m	density kg/m^3	S-wave velocity m/s	P-wave velocity m/s	earth press. coeff.	reference strain ‰	soil sample
1	sandy silt (LS1+LS2)	12	1800	200	516	0.7	0.39	S11-C3
2	silty clay	21.5	1850	190	491	0.7	0.48	
3	sandy gravel	25.0	1900	240	759	0.8	0.39	S11-C3
4	silty clay	31.5	1900	280	723	0.7	0.49	
5	sandy gravel	71.5	1975	385	994	0.7	100	
6	silty clay	111.5	2125	595	1536	0.7	100	
	Bedrock	> 111.5	2200	700	1807	0.7		

832

833　**Table 5.** Normalized shear modulus reduction curves G/G_0 obtained using RC tests.

Soil sample	S2-C2		S3-C3		S10-C3	
Soil type	sandy silt/gravel		silty clay		deep silty clay	
Shear ref. strain	$\gamma_{r0} = 0.39‰$		$\gamma_{r0} = 0.48‰$		$\gamma_{r0} = 0.49‰$	
	shear strain	G/G_0	shear strain	G/G_0	shear strain	G/G_0
	%		%		%	
	0.00015	1.000	0.00010	1.000	0.000042	1.000
	0.00030	1.000	0.00020	1.000	0.000075	1.000
	0.00064	1.000	0.00033	1.000	0.000165	1.000
	0.00097	0.995	0.00061	0.996	0.000315	1.000
	0.00161	0.982	0.00106	0.985	0.000550	1.001
	0.00245	0.966	0.00175	0.961	0.000784	1.001
	0.00406	0.926	0.00328	0.925	0.001209	1.001
	0.00583	0.890	0.00583	0.868	0.001561	1.001
	0.01159	0.810	0.00905	0.819	0.002307	1.002
	0.02178	0.692	0.01688	0.719	0.003178	0.996
	0.04659	0.509	0.03310	0.529	0.004950	0.968
	0.07419	0.400	0.07133	0.331	0.006578	0.947
	0.20062	0.197			0.008409	0.928
					0.014088	0.838
					0.022048	0.719
					0.038053	0.550
					0.074181	0.390
					0.199728	0.208
					0.289764	0.163

834

835

836   **Table 6.** Liquefaction parameters used to calibrate CTX test curves

			Soil sample			
			S11-C1-1	S11-C1-2	S11-C3-2	S11-C3-3
Density	ρ	kg/m^3	1950	1950	2050	2050
S-wave velocity	v_s	m/s	175	175	152	152
P-wave velocity	v_p	m/s	2480	2480	2149	2149
Reference strain	γ_r	‰	0.11	0.11	0.15	0.15
Friction angle	α	°	29	29	32	32
Dilatation angle	ϕ_p'	°	25	25	26	26
Cell pressure	p_0	kN/m^2	300	300	300	300
Back pressure	u_0	kN/m^2	200	200	200	200
	c_1		5.0	4.9	5.2	5.0
	S_1		0.005	0.005	0.005	0.005
	p_1		0.4	0.4	0.4	0.4
	p_2		0.6	0.6	0.6	0.6
	w_1		5.9	6.2	6.5	6.0

837

838   **Table 7.** Peak ground acceleration in *x*- and *y*-direction for the different water table depth z_w

		Soil profile										
		C1				C2				C3		
	z_w	a_x	a_y		z_w	a_x	a_y		z_w	a_x	a_y	
	m	m/s^2	m/s^2		m	m/s^2	m/s^2		m	m/s^2	m/s^2	
TSA		1.40	1.37	TSA		1.46	1.60	TSA		1.55	1.61	
ESA	6.8	1.68	1.61	ESA	6.2	2.23	1.81	ESA	3.7	2.10	1.87	
ESA	5.8	1.68	1.59	ESA	5.2	2.23	1.81	ESA	2.7	**3.21**	2.27	
ESA	4.8	1.72	1.63	ESA	4.2	2.22	1.72	ESA	1.7	**4.02**	2.22	

839

840

FIGURE CAPTIONS
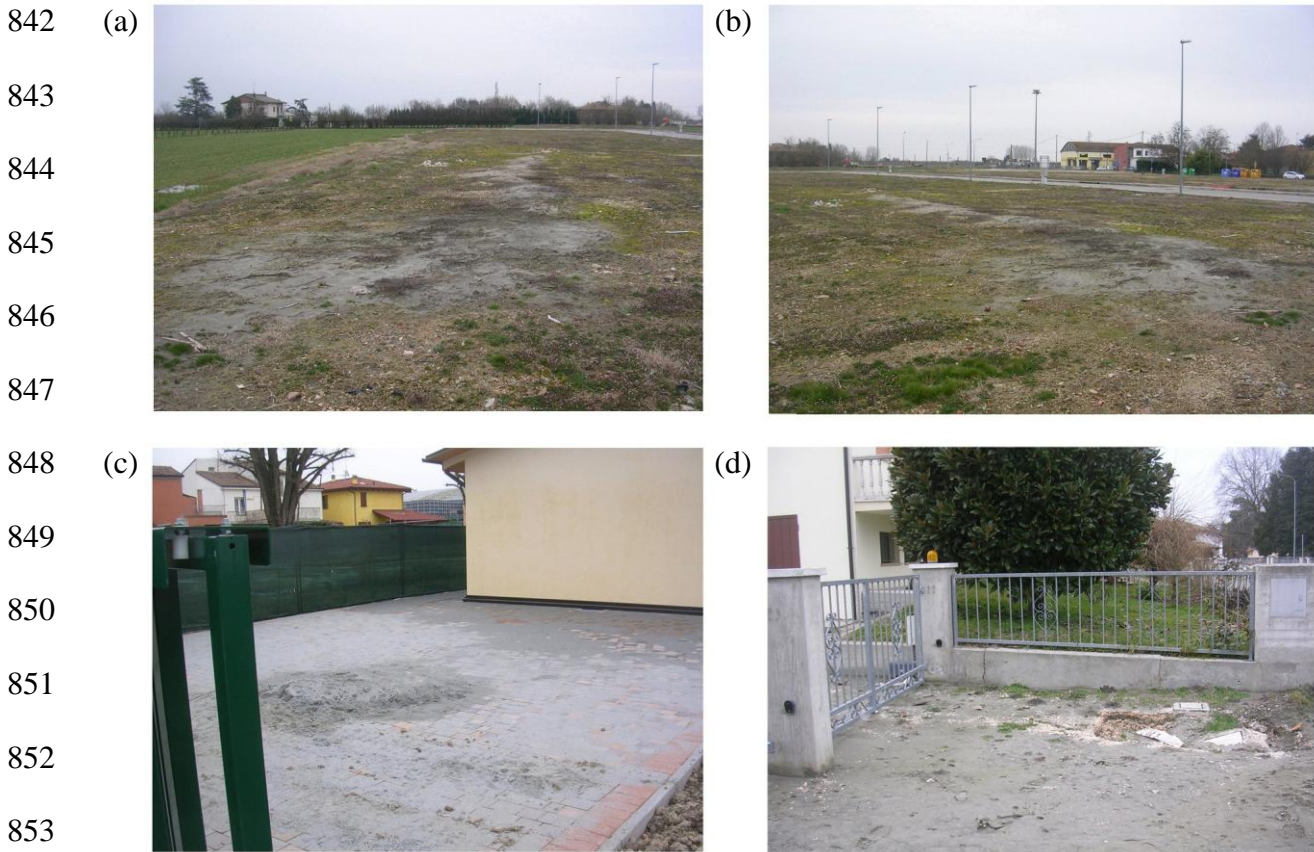
Figure 1. Liquefaction effects observed at San Carlo village after the 20 May 2012 M_w 5.9 earthquake: a, b) evidences of clay spread out on free field; c, d) evidence of clays spread out from building foundations causing damage to structures.

864   (a)
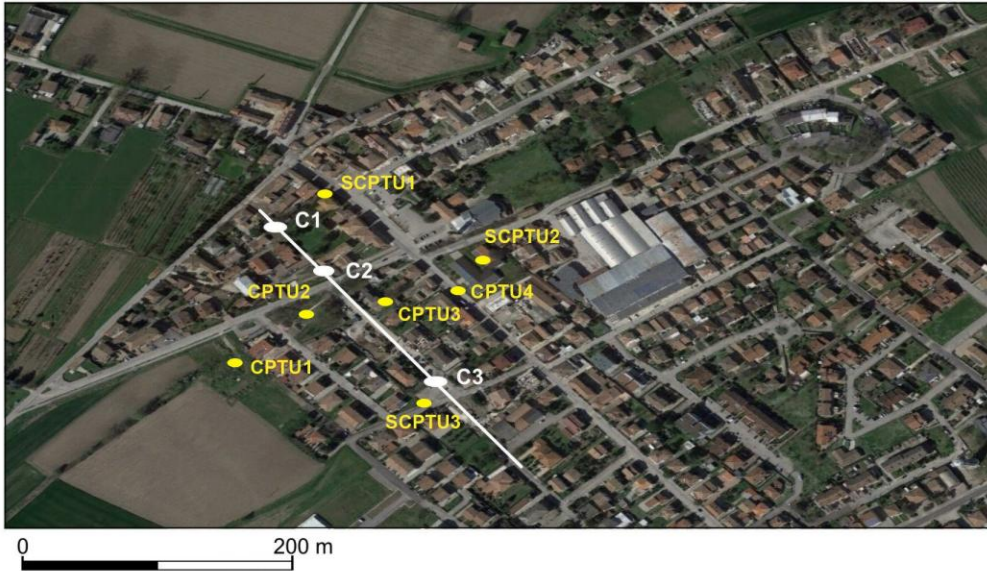
872   (b)
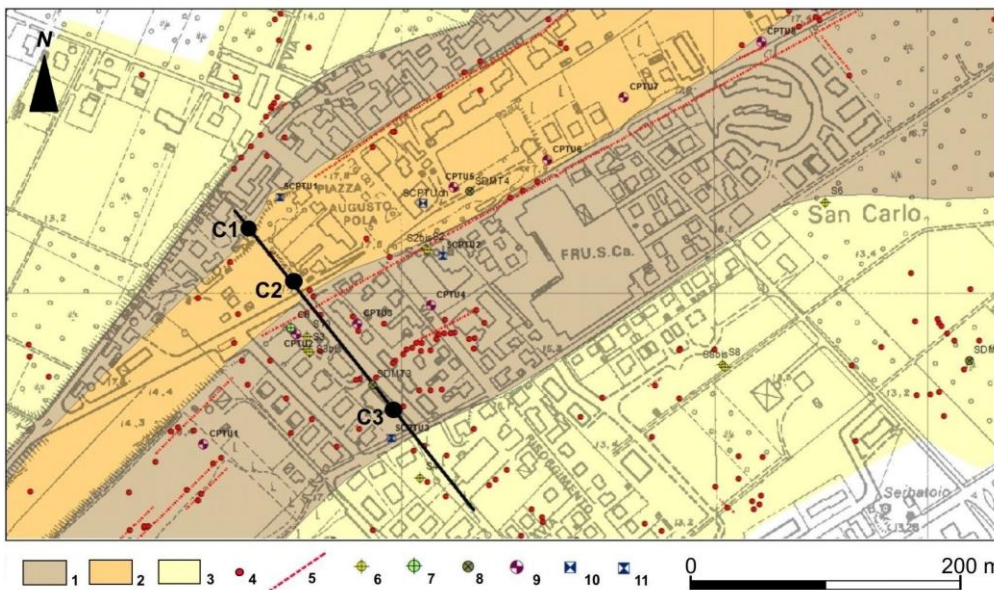
880   (c)
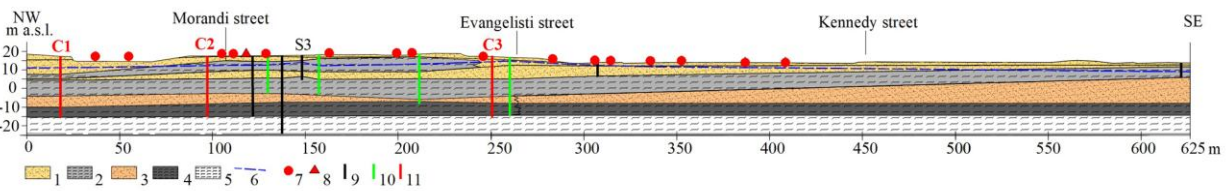
Figure 2. (a) Google Earth satellite view of the San Carlo village with trace of geological cross

section and location of modelled soil columns. (b) geological map of the San Carlo village: 1)

deposits of river channel; 2) deposits of river banks; 3) deposits of alluvial plain; 4) liquefaction

44

887   sand boil; 5) liquefaction trench; 6) borehole with samples; 7) borehole without samples; 8)

888   Seismic DilatoMeter Test (SDMT); 9) Cone Penetration Test with piezocone (CPTU); 10)

889   Seismic Cone Penetrometric Test with piezocone (SCPTU); 11) Seismic Cone Penetrometric

890   Test (SCPT). (c) Geological cross section: 1) Holocene liquefiable deposits; 2) Holocene not

891   liquefiable deposits; 3) Pleistocene liquefiable deposits; 4) Pleistocene non liquefiable deposits;

892   5) not classified Pleistocene deposits; 6) water table; 7) liquefaction sand boil; 8) liquefaction

893   trench; 9) borehole; 10) CPTU or SCPT test; 11) modelled soil columns.

894
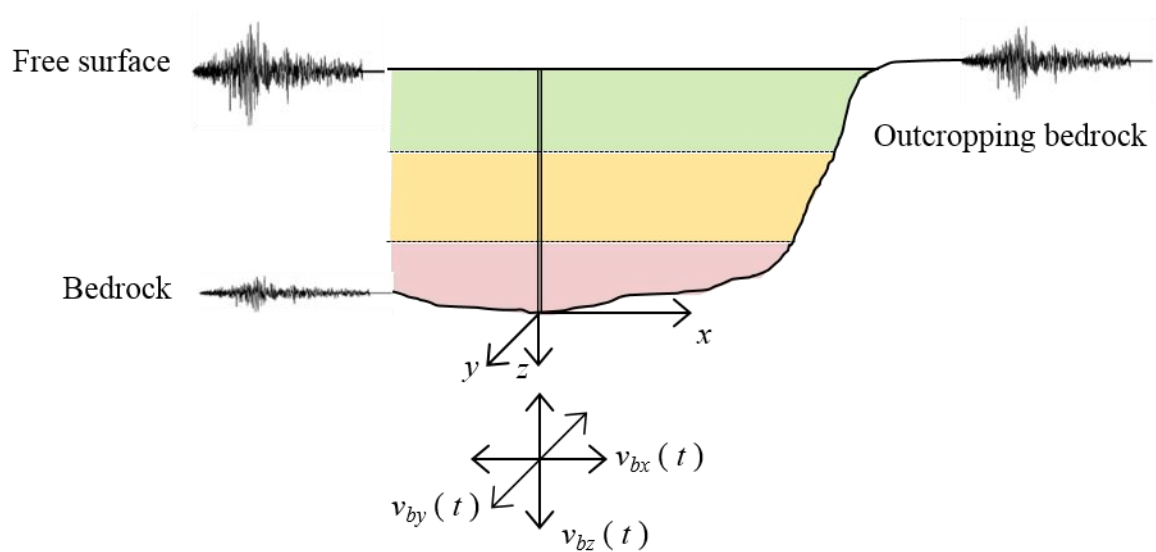
895

896   **Figure 3.** Spatial discretization of a horizontally layered soil. The seismic loading applied at the

897   bedrock level is a deconvolved outcropping signal in terms of velocity.

45

898
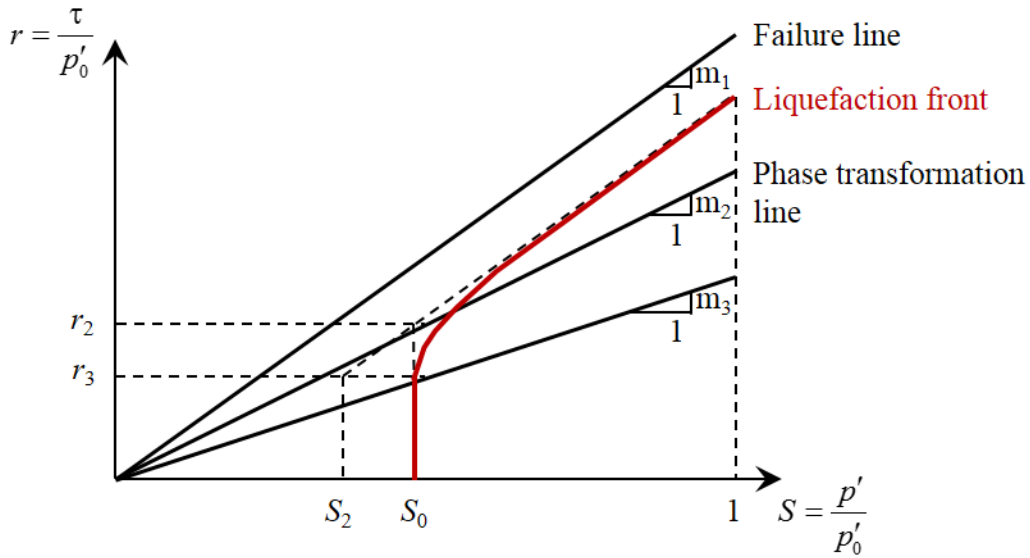
Figure 4. Liquefaction front $r(S)$, where r is the deviatoric stress ratio and S is the state

900 variable.

901
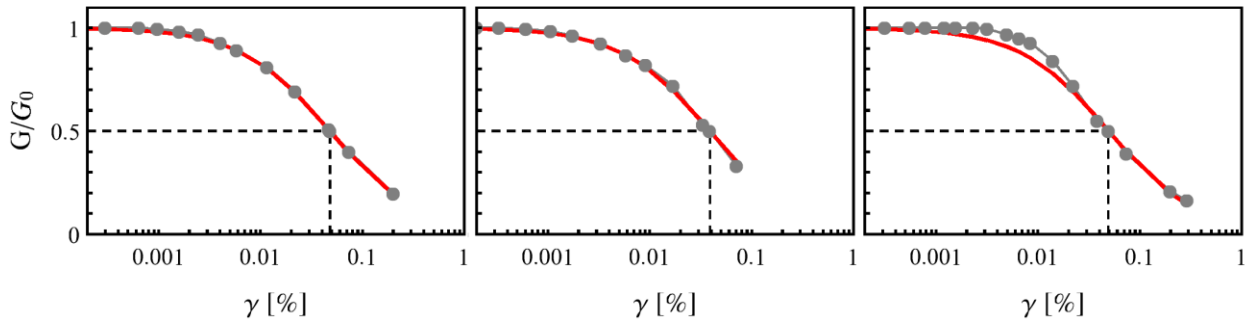
902

903 **Figure 5.** Normalized shear modulus reduction curves obtained using RC test results (markers)

904 and fitted using the hyperbolic model (solid line), for soil samples S2-C2 (left) having reference

905 shear strain $\gamma_{r0} = 0.48‰$, S3-C3 (middle) having $\gamma_{r0} = 0.39‰$ and S10-C3 (right) having

906 $\gamma_{r0} = 0.49‰$.
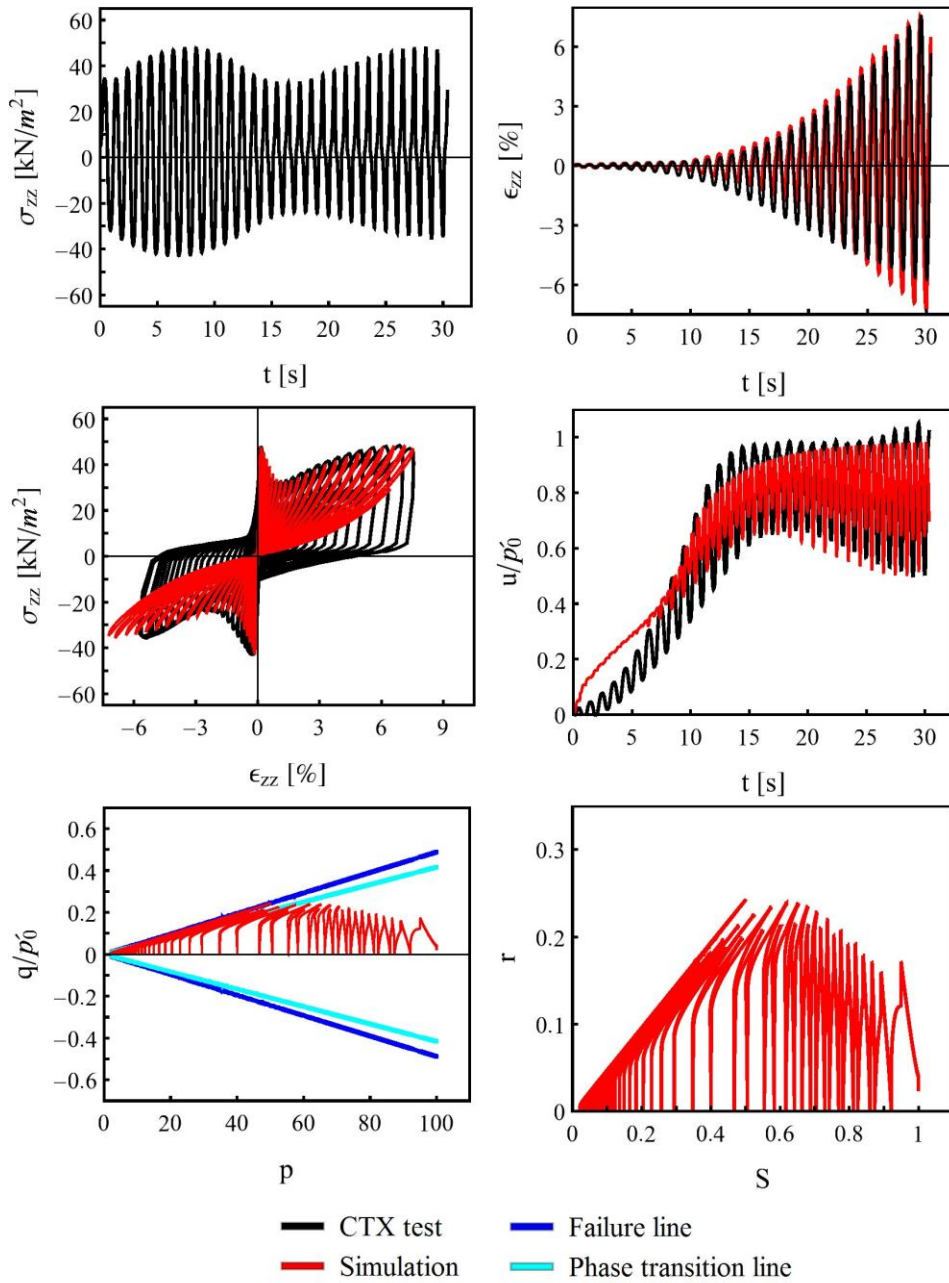
Figure 6. Fitting of cyclic Consolidated Undrained triaxial test curves to calibrate liquefaction parameters, for S11-C1-2 soil sample in LS1 liquefiable soil layer.

Figure 7. Fitting of cyclic Consolidated Undrained triaxial test curves to calibrate liquefaction parameters, for S11-C3-3 soil sample in LS2 liquefiable soil layer.

Figure 8. Three components of the incident motion applied at the soil-bedrock interface in terms of acceleration. The peak acceleration is 2.54 m/s^2 in x-direction, 1.51 m/s^2 in y-direction and 0.33 m/s^2 in z-direction.

919

Figure 9. Profiles with depth of maximum shear strain and stress, horizontal velocity and acceleration, during the seismic event, for different water table depth and for TSA conditions in the C1 soil column. The horizontal dashed lines indicate the depth where the shear stress-strain loops are analyzed.

924

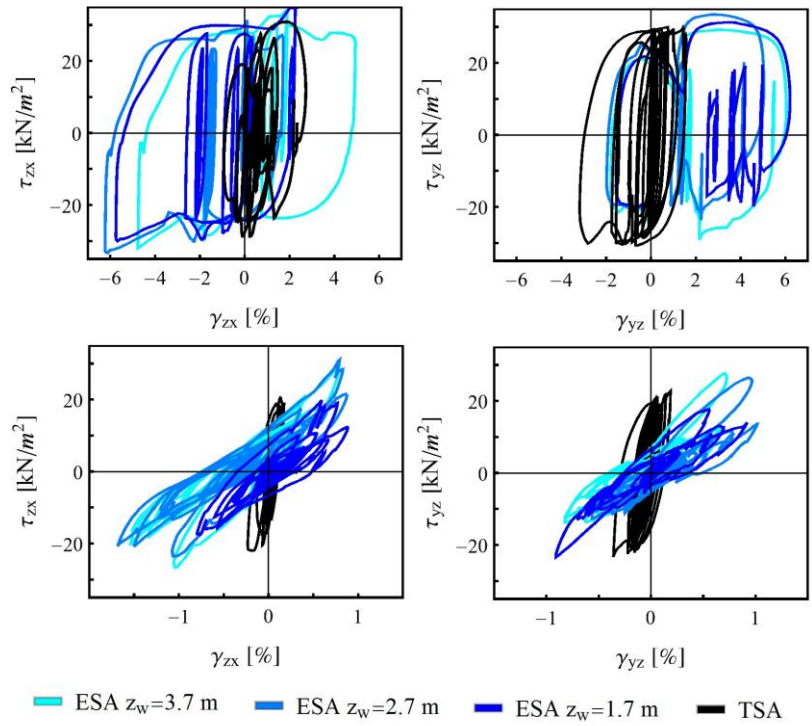**Figure 10.** Hysteresis loops in C1 soil profile for different water table depth and for TSA conditions: (top) at 21.5 m in a non liquefiable soil layer; (bottom) at 13 m in LS2 liquefiable soil layer.

Figure 11. Profiles with depth of maximum shear strain and stress, horizontal velocity and acceleration, during the seismic event, for different water table depth and for TSA conditions in the C2 soil column. The horizontal dashed lines indicate the depth where the shear stress-strain loops are analyzed.

933

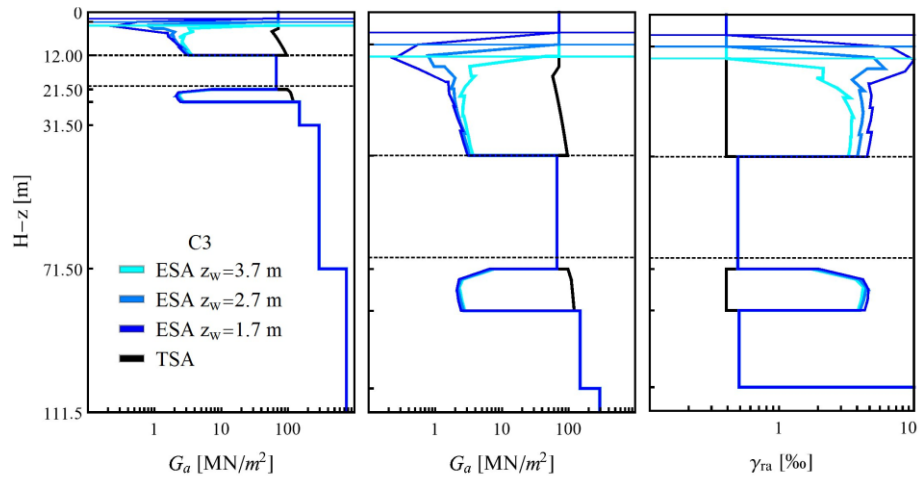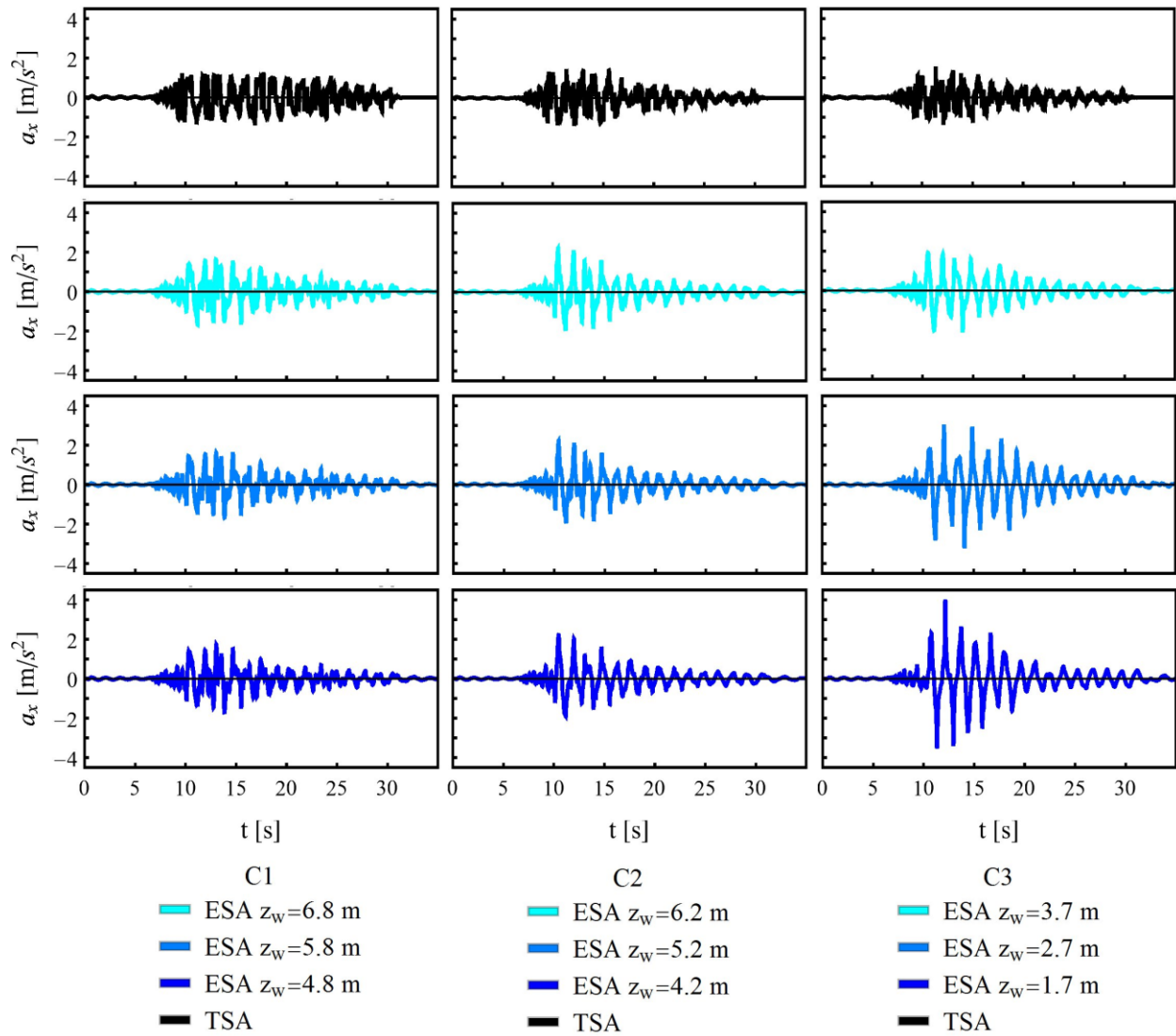**Figure 12.** Hysteresis loops in C2 soil profile for different water table depth and for TSA conditions: at 9 m (top) and at 12.5 m (bottom) in LS2 liquefiable soil layer.

Figure 13. Profiles with depth of maximum shear strain and stress, horizontal velocity and acceleration, during the seismic event, for different water table depth and for TSA conditions in the C3 soil column. The horizontal dashed lines indicate the depth where the shear stress-strain loops are analyzed.

942

Figure 14. Hysteresis loops in C3 soil profile for different water table depth and for TSA conditions: (top) at 20.5 m in a non liquefiable soil layer; (bottom) at 12 m in LS1+LS2 liquefiable soil layer.

946

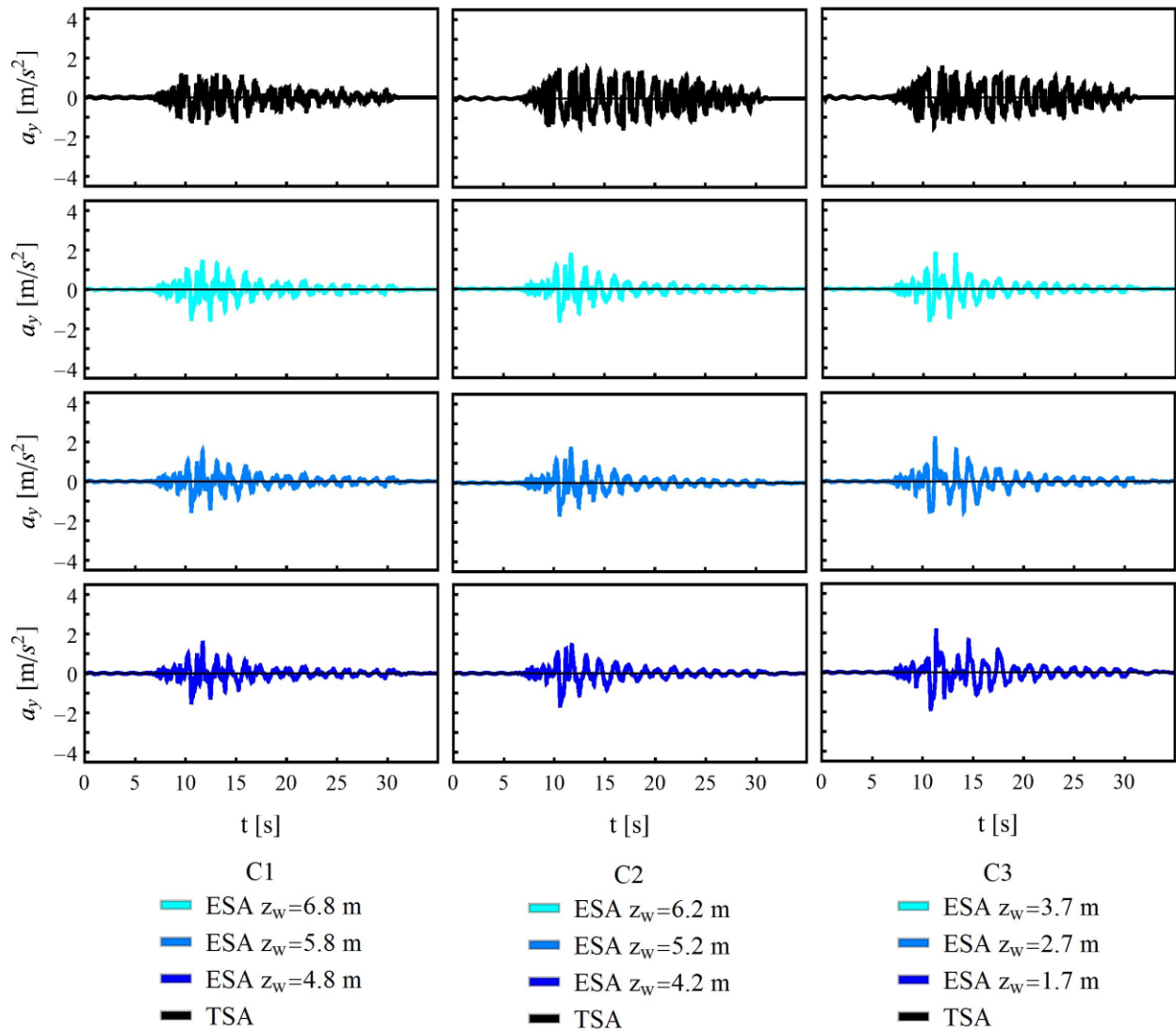947

Figure 15. Profile with depth of minimum shear modulus (left), during the seismic event, with zoom in the first soil layers (middle) and profile with depth of the maximum reference shear strain, for different water table depth and for TSA conditions, in the C3 soil profile. The horizontal dashed lines indicate the depth where the shear stress-strain loops are analyzed.

952

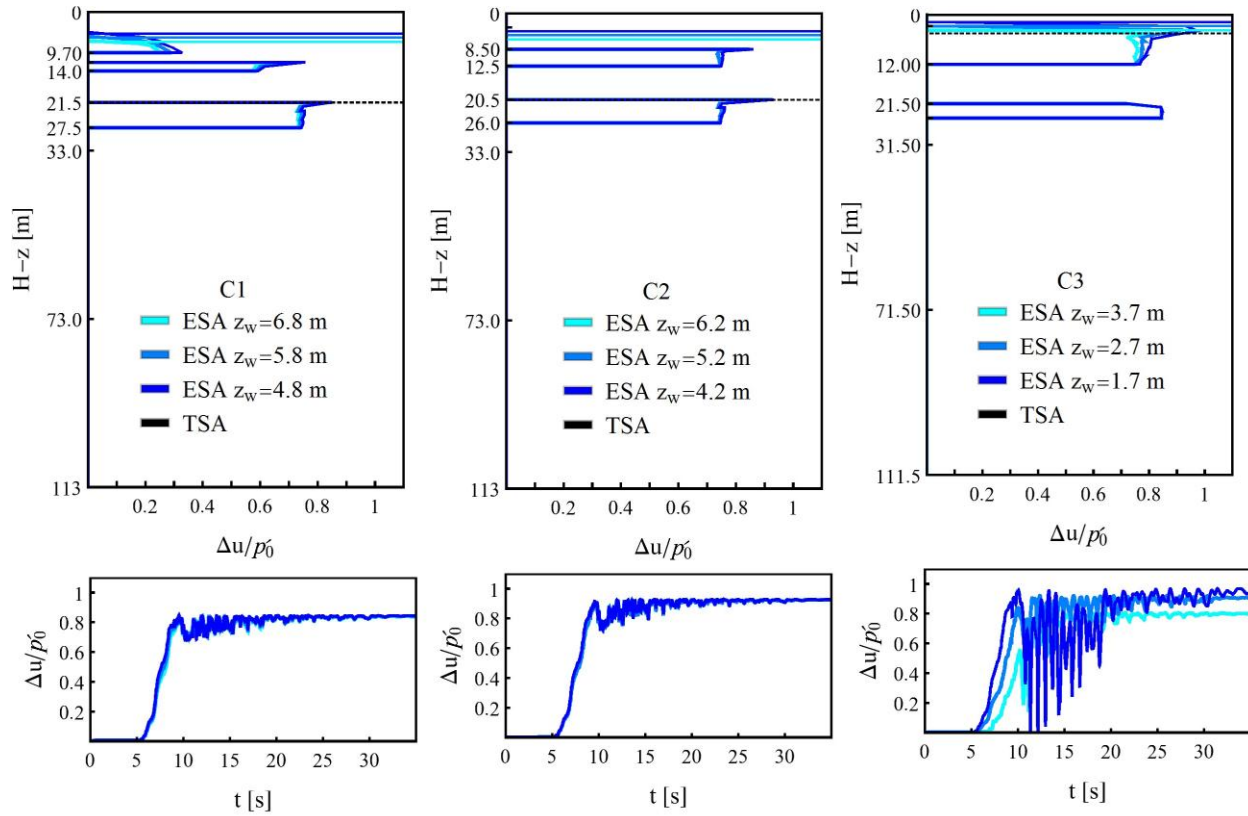**Figure 16.** Acceleration time history at the ground surface for C1 (left), C2 (middle) and C3

(right) soil profiles, in *x*-direction, for different water table depth and for TSA conditions.

Figure 17. Acceleration time history at the ground surface for C1 (left), C2 (middle) and C3 (right) soil profiles, in *y*-direction, for different water table depth and for TSA conditions.

958

Figure 18. Excess pore water pressure, normalized with respect to the average effective pressure, for different water table depth, in C1 (left), C2 (middle) and C3 (right) soil columns: (top) Profiles with depth of maximum value during the seismic event. The horizontal dashed lines indicate the depth where the time histories are analyzed. (bottom) Time history: at 21.5 m (LS1) in C1 soil profile, at 20.5 m (LS2) in C2 soil profile and at 4.5 m (LS1+LS2) in C3 soil profile, for $z_w = 3.7$ m, at 3.5 m for $z_w = 2.7$ m and $z_w = 1.7$ m.